

PAPER • OPEN ACCESS

# Bayesian inference of radial impurity transport in the pedestal of ASDEX Upgrade discharges using charge-exchange spectroscopy

To cite this article: T. Gleiter *et al* 2025 *Nucl. Fusion* **65** 056010

View the [article online](#) for updates and enhancements.

You may also like

- [EDA H-mode in ASDEX Upgrade: scans of heating power, fuelling, and plasma current](#)  
L. Gil, T. Pütterich, C. Silva et al.
- [Low frequency  \$m = 1\$  modes during standard and improved confinement scenarios in W7-X](#)  
Dario Cipciar, Carsten Killer, Christian Brandt et al.
- [Strong electron temperature stiffness induced by broad-band turbulence in high poloidal beta plasmas on EAST](#)  
F. Chen, Y.C. Hu, Y.D. Li et al.

# Bayesian inference of radial impurity transport in the pedestal of ASDEX Upgrade discharges using charge-exchange spectroscopy

T. Gleiter<sup>1,2,\*</sup>, R. Dux<sup>1</sup>, F. Sciortino<sup>3</sup>, T. Odstrčil<sup>4</sup>, D. Fajardo<sup>1</sup>, C. Angioni<sup>1</sup>, J. Buchner<sup>5</sup>, R.M. McDermott<sup>1</sup>, T. Hayward-Schneider<sup>1</sup>, G.F. Harrer<sup>6,7</sup>, M. Faitsch<sup>1</sup>, M. Griener<sup>1</sup>, R. Fischer<sup>1</sup>, E. Wolfrum<sup>1</sup>, U. Stroth<sup>1,2</sup> and the ASDEX Upgrade Team<sup>a</sup>

<sup>1</sup> Max Planck Institute for Plasma Physics, Garching, Germany

<sup>2</sup> Physics Department, TUM School of Natural Sciences, Technical University of Munich, Garching, Germany

<sup>3</sup> Proxima Fusion, Munich, Germany

<sup>4</sup> General Atomics, San Diego, CA, United States of America

<sup>5</sup> Max Planck Institute for Extraterrestrial Physics, Garching, Germany

<sup>6</sup> Institute of Applied Physics, Vienna University of Technology, Vienna, Austria

E-mail: [tabea.gleiter@ipp.mpg.de](mailto:tabea.gleiter@ipp.mpg.de)

Received 8 October 2024, revised 31 January 2025

Accepted for publication 28 February 2025

Published 2 April 2025



## Abstract

We present a novel framework for quantifying radial impurity transport in the pedestal of ASDEX Upgrade (AUG) discharges. Our method is based on charge-exchange recombination spectroscopy measurements of line radiation from multiple impurity charge states, each along a radially distributed line-of-sight array in steady-state plasmas. Inverse inference based on the diffusive-convective transport solver Aurora combined with a synthetic diagnostic enables us to separate diffusive and convective transport contributions and to derive the impurity density and charge state distribution profiles. Robust uncertainty quantification is provided as the full probability distribution of the parameters is obtained according to Bayesian statistics with the use of a nested sampling algorithm. The approach allows for a high radial resolution and data quality due to the steady-state plasma, but requires data from multiple impurity charge states. It is, therefore, particularly suitable for impurity transport studies in the region of steep edge gradients. In this paper, we present thorough tests of the method based on synthetic data. Furthermore, we show an application to AUG measurement data, inferring the pedestal neon transport in the quasi-continuous exhaust (QCE) regime without large edge-localized modes. The comparison of the transport result with neoclassical simulations shows a clear contribution

<sup>7</sup> Current address: Department of Physics, School of Science, Hampton University, VA, United States of America.

<sup>a</sup> See Zohm *et al* 2024 (<https://doi.org/10.1088/1741-4326/ad249d>) for the ASDEX Upgrade Team.

\* Author to whom any correspondence should be addressed.



Original Content from this work may be used under the terms of the [Creative Commons Attribution 4.0 licence](https://creativecommons.org/licenses/by/4.0/). Any further distribution of this work must maintain attribution to the author(s) and the title of the work, journal citation and DOI.

of turbulent diffusion in the QCE pedestal. This supports the hypothesis of additional transport associated with the predicted high- $n$  ballooning-unstable region and the observed quasi-coherent mode.

**Keywords:** ASDEX Upgrade, impurity transport, pedestal, charge-exchange spectroscopy, Bayesian inference, nested sampling, QCE regime

(Some figures may appear in colour only in the online journal)

## 1. Introduction

Understanding the radial impurity transport in reactor-relevant confinement regimes is essential for predicting and tailoring the energy confinement and power exhaust properties of future tokamaks. Together with ionization and recombination processes, transport determines the impurity density, the charge state distribution, and thus the radiation efficiency throughout the plasma. Whereas only small impurity concentrations are tolerable in the core to minimize radiative energy losses (especially due to high- $Z$  impurities such as W eroded from the wall) and fuel dilution, the plasma edge of a reactor is likely to require targeted impurity seeding (e.g. of Xe, Kr, Ar, Ne or  $N_2$ ) to protect the vessel via radiative cooling and divertor detachment [1, 2].

Of particular importance for the integration of these objectives is the core-edge connecting pedestal region. In the high-confinement regime (H-mode) with type-I edge-localized modes (ELMs), a transport barrier suppresses turbulence at the plasma edge [3] and the pedestal impurity transport in inter-ELM phases has been observed to be close to the neo-classical, i.e. collisional, level [4]. But little is known in this respect about the various potentially reactor-relevant ELM-free, ELM-suppressed and small-ELM regimes, such as the quasi-continuous exhaust (QCE) regime, described in [5]. They differ in the MHD and turbulent instabilities present [6], which increase the transport sufficiently to keep their pedestals away from the peeling-ballooning boundary and may also impact the impurity transport. Experimental quantification of the impurity transport in these regimes is necessary to scale them to larger tokamaks with different pedestal kinetic profiles. For example, it is expected for ITER [7], and has been demonstrated in high heating power JET plasmas [8], that larger pedestal ion temperature gradients than typical in current devices can reverse the direction of the neoclassical convection to an outward drift. As predictions must take such effects into account, they cannot be based on simple assessments, e.g. of impurity density profiles or confinement times. Rather, they require analyses of the underlying transport mechanisms in the common terms of diffusion and convection coefficients ( $D$  and  $v$ ) [9, 10], and their separation into collisional and turbulent contributions via comparison with neoclassical transport modeling. However, the inference task is difficult in the pedestal due to the steep gradients, requiring well aligned, high quality, and radially dense data, due to the presence of non-fully stripped impurity charge states, calling for accurate atomic ionization and recombination data, and due to the closeness

to the scrape-off-layer (SOL), where impurity densities have complex 3-D distributions.

If the total impurity density profile summed over all charge states can be measured, the transport coefficient profiles, when assumed equal for all prevailing charge states, can be directly assessed based on the flux-gradient relation, as, for example, in [11, 12]. This technique uses intentional perturbation of the impurity content, e.g. by laser-blow-off (LBO), pellet injection, gas puff or ICRF heating modulation, and observation of the subsequent equilibration of the total impurity density. However, it is mostly applicable for fully stripped low- $Z$  impurities in the core, whereas at the plasma edge and for high- $Z$  impurities, total impurity density measurements are difficult and studies using the flux-gradient method require assumptions or modeling of the charge state distribution, as, for example, in [13]. Alternatively, additional diagnostics, such as tomographic inversion of soft x-ray (SXR) spectroscopy, are often used to constrain  $D$  and  $v$  in the system of transport equations for the charge state densities, as, for example, in [14, 15].

A more straightforward approach can be used if density profiles of  $\geq 2$  different impurity charge states can be measured, best with charge-exchange recombination spectroscopy (CXRS), in a steady-state plasma without impurity modulation [16, 17]. The system of transport equations coupled via ionization and recombination processes is simplified by the steady-state condition such that data of two charge states is sufficient to determine  $D$  and  $v$  in the confined plasma without impurity sources. This approach has rarely been used due to the specific diagnostic requirements and because it is not well applicable in the core as it requires the presence of multiple measurable charge states. It is, however, particularly advantageous for the steep edge gradient region as it allows data to be averaged in time. Thus, the data quality can be improved with neutral beam injection (NBI) dips, i.e. short off periods, for passive spectra subtraction and the radial resolution can be enhanced using radial plasma sweeps as in [18]. Furthermore, the trace limit condition, which is important to assume unaltered transport in experiments with time evolving impurity concentration, is not imposed, allowing higher impurity content to yield better signals. The required steady-state condition is easily fulfilled in most scenarios with small or no ELMs.

Studies relying on the coupled system of transport equations as forward model mapping from parameter space to data space deal with a complex non-linear inverse problem. Many previous analyses used  $\chi^2$  fitting techniques, e.g. with Levenberg–Marquardt minimization, see, for

example, [16, 19, 20], which are unable to deal with non-Gaussian error statistics and potential multimodality. A more robust uncertainty quantification is reached when inferring the full probability distribution of the parameters according to Bayesian statistics, but this significantly increases the computational demand [21]. To this end, the Aurora code [22, 23] was developed, based on the numerical impurity transport solver STRAHL [24], to optimize the runtime of the forward model. Moreover, specifically for the steady-state case, an analytical forward model was developed in [17] and is included in the Aurora package. In addition, a new module ‘ImpRad’ for Bayesian impurity transport inferences was implemented within the One Modeling Framework for Integrated Tasks (OMFIT) [25]. It entails the nested sampling [26, 27] algorithm MultiNest [28, 29], which is capable of handling non-differentiable models and multimodality. First applications can be found in [30–33].

In this work, we present a novel framework for inferences of radial  $D$  and  $v$  profiles in the pedestal of ASDEX Upgrade (AUG) discharges, using CXRS data of multiple charge states in stationary plasmas without impurity modulation. The framework builds on the AUG CXRS system and previous work on Bayesian impurity transport inference as detailed above. In particular, the diagnostic setup was refined and the ‘ImpRad’ module was extended to handle the steady-state AUG data. Moreover, special effort was put into the selection of suitable free parameter sets, prior distribution and data likelihood definitions, and the Bayesian sampler settings to analyze the specific data set. The details of the framework, i.e. the diagnostic setup, the forward model and the inverse inference procedure, are introduced in section 2. Thereafter, in section 3, we show tests with realistic synthetic data, in particular assessing the parameterization of the  $D$  and  $v$  profiles, and the impact of potential data perturbations and model errors.

Finally, in section 4, we present an application to AUG measurement data with an analysis of Ne transport in the pedestal of a QCE discharge. The QCE regime has small—previously labeled as type-II—ELM activity and does not show impurity accumulation in AUG [34]. Our finding of diffusion well above the neoclassical level supports the hypothesis of additional impurity transport in the QCE pedestal, which may be connected to the high- $n$  ballooning-like instability [35] and the observed quasi-coherent mode (QCM) [36, 37] at the pedestal foot.

## 2. Inference framework

### 2.1. General principle

The continuity equation for the impurity density  $n_{I,Z}$  of each charge state  $Z$  is

$$\frac{\partial n_{I,Z}}{\partial t} = -\nabla \cdot \vec{\Gamma}_{I,Z} + Q_{I,Z}, \quad (2.1)$$

with the impurity flux density  $\vec{\Gamma}_{I,Z}$  and the source term  $Q_{I,Z}$ . The latter is determined by ionization and recombination

processes from neighboring charge states, yielding a coupled system of equations.

To obtain equations for flux surface averaged radial impurity transport, we use the radial coordinate

$$r = \sqrt{\frac{V}{2\pi^2 R_{\text{axis}}}}, \quad (2.2)$$

for the flux surface enclosing the volume  $V$ , where  $R_{\text{axis}}$  is the major radius of the magnetic axis. The impurity distribution is assumed to be poloidally symmetric, such that  $n_{I,Z}$  and  $Q_{I,Z}$  are approximately constant on a flux surface. Impurities with rather low charge and mass, as they are used with this framework, e.g. Ne or Ar, are indeed less prone to asymmetries due to the centrifugal force, but some asymmetries due mainly to friction remain as was shown in [38]. However, they are not included as they are not measured. Further, the radial impurity flux density  $\Gamma_{I,Z}^r$  is parameterized by the diffusion and convection coefficients  $D$  and  $v$ , which are flux surface averaged over their poloidal variations due to the varying magnetic field strength. Thus,

$$\Gamma_{I,Z}^r = -D \frac{\partial n_{I,Z}}{\partial r} + v n_{I,Z}, \quad (2.3)$$

such that the flux surface averaged transport equation reads

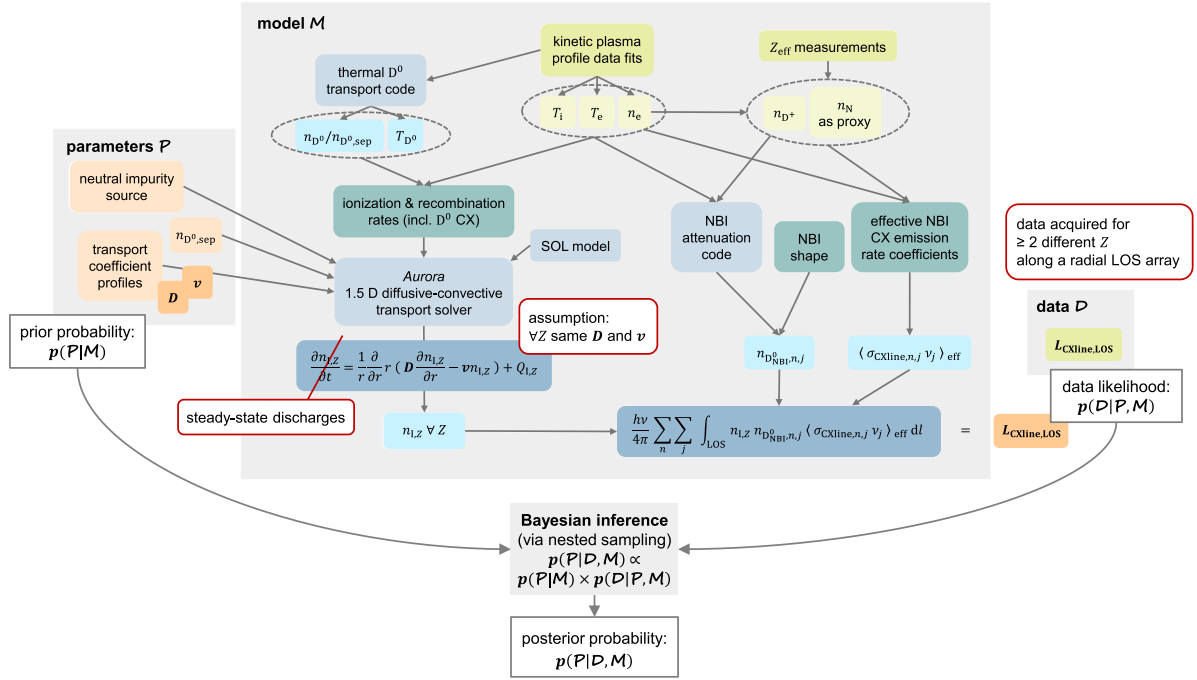
$$\frac{\partial n_{I,Z}}{\partial t} = \frac{1}{r} \frac{\partial}{\partial r} r \left( D \frac{\partial n_{I,Z}}{\partial r} - v n_{I,Z} \right) + Q_{I,Z}. \quad (2.4)$$

The system of radial equations can be solved numerically for all impurity charge state densities with 1.5-D impurity transport solvers, such as STRAHL [24] or Aurora [22, 23]. They require  $D$ ,  $v$ , the magnetic equilibrium and kinetic profiles of the plasma, the atomic rates for relevant ionization and recombination processes, and a model for SOL impurity sources and losses as inputs.

For an inverse inference of  $D$  and  $v$ , additional information on the impurity densities is required. In the case of a steady-state plasma, the knowledge of the density profiles of  $\geq 2$  charge states reduces the number of unknowns to less than the number of equations. This is based on the assumption of equal  $D$  and  $v$  for all charge states, which is justified if charge states with similar  $Z$  prevail. Yet, the system of equations is non-linear and includes additional unknowns, in particular the sources of the neutral impurity and of thermal neutral deuterium in the SOL, which involve recycling and are difficult to measure. For these reasons, complex non-Gaussian error statistics as well as multimodality can occur. Thus, it is beneficial to infer the full probability distribution of the parameters according to Bayesian statistics, i.e.

$$p(\mathcal{P}|\mathcal{D}, \mathcal{M}) = \frac{p(\mathcal{D}|\mathcal{P}, \mathcal{M})p(\mathcal{P}|\mathcal{M})}{\int p(\mathcal{D}|\mathcal{P}, \mathcal{M})p(\mathcal{P}|\mathcal{M})d\mathcal{P}} \propto p(\mathcal{D}|\mathcal{P}, \mathcal{M})p(\mathcal{P}|\mathcal{M}). \quad (2.5)$$

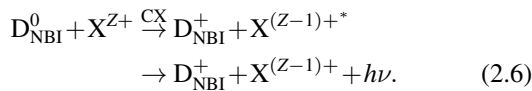
Here,  $p(\mathcal{P}|\mathcal{D}, \mathcal{M})$  is the posterior probability for a parameter set  $\mathcal{P}$  given the data  $\mathcal{D}$  and the model  $\mathcal{M}$ . According to Bayes’



**Figure 1.** Schematic of the inference framework, as described in section 2. The plasma equilibrium, which is needed for all parts of the inference framework, is obtained from routinely written EQH/EQI shotfiles. They contain the output of CLISTE runs based on magnetic data.

theorem it is proportional to the product of the data likelihood  $p(\mathcal{D}|\mathcal{P}, \mathcal{M})$  with the prior probability of the parameter set  $p(\mathcal{P}|\mathcal{M})$ , which is assigned according to previous knowledge, e.g. physical reasoning. Since an analytical calculation is not possible, the posterior distribution must be sampled. Our sampling method is presented in section 2.4.

The impurity densities of multiple charge states are obtained with the CXRS diagnostic, using a radial array of toroidally looking lines-of-sight (LOS). Line radiance of an impurity X is observed after charge exchange (CX) with neutral deuterium  $D_{NBI}^0$  from the NBI when the electron decays from the initial excited state, i.e.



The light captured by each LOS is given by the integration along the intersection region of LOS and neutral beam,

$$L_{CXline,LOS} = \frac{h\nu}{4\pi} \sum_n \sum_j \int_{LOS} n_{1,Z} n_{D_{NBI}^0,n,j} \langle \sigma_{CXline,n,j} v_j \rangle_{eff} dl, \quad (2.7)$$

where  $n_{D_{NBI}^0,n,j}$  are the densities of the NBI neutrals with velocity components  $j$  and excitation states  $n$ , and  $\langle \sigma_{CXline,n,j} v_j \rangle_{eff}$  are the effective CX emission rate coefficients. The CX cross sections  $\sigma_{CXline,n,j}$  are a function of the relative velocity  $v_j$  between the colliding species, and  $\langle \rangle$  signifies the integration over the velocity distributions of the species. Thus, the impurity emission observed with CXRS is directly related to the impurity densities. In addition to the impurity transport solver,

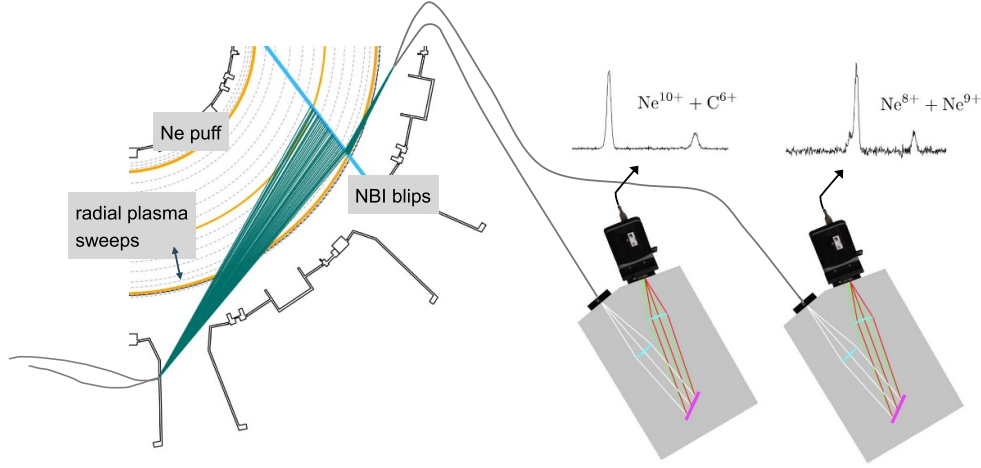
the above equation is included as a synthetic diagnostic in the forward model  $\mathcal{M}$  mapping from parameter space to data space. The neutral beam density is calculated with a beam attenuation code and a beam shape model, and the effective CX emission rate coefficients are retrieved from atomic data.

Figure 1 shows an overview of the inference framework. The diagnostic setup, the forward model including the synthetic diagnostic, and the inverse inference are specified in more detail in sections 2.2, 2.3 and 2.4, respectively.

## 2.2. CXRS diagnostic setup

Figure 2 shows a schematic of the diagnostic setup. The transport analyses in this work focus on Ne, although the framework can, in principle, be applied to other impurities, e.g. Ar or N<sub>2</sub>, as well. Ne is advantageous due to its moderate atomic number (10), which is high enough to have significant densities of non-fully stripped ions throughout the pedestal, in particular the He- and H-like charge states, but low enough to provide good interpretability of the CXRS signal due to known effective CX emission rate coefficients. The experimental setup is similar to the one in [16], which also uses the AUG CXRS system to measure multiple Ne charge states. Due to the CX-reaction that induces the observed line radiation, stated in equation (2.6), the density of the Ne<sup>Z+</sup> charge state, with which we will further refer to the data, is represented by the radiance of a Ne<sup>(Z-1)+</sup> transition. The spectral lines used to provide information about the Ne<sup>10+</sup>, Ne<sup>9+</sup> and Ne<sup>8+</sup> densities are NeX  $n = 11 \rightarrow 10$  at 524.88 nm, NeIX  $n = 14 \rightarrow 12$  at 610.44 nm and NeVIII  $n = 10 \rightarrow 9$  at 606.82 nm. Additional CX-lines (NeVIII  $n = 13 \rightarrow 11$  at 606.41 nm and carbon CVI





**Figure 2.** Schematic of the diagnostic setup, as described in section 2.2. The top-down view of a torus segment shows the toroidally looking LOS of the core and edge CXRS systems (dark green), from their intersection points with beam 3 of NBI box 1 in sector 16 (blue) to the respective optical heads. The plasma is indicated by the magnetic axis and separatrix (orange). The LOS of each optical head are alternately imaged onto 2 spectrometers, which observe spectral lines that contain information on the densities of the 3 charge states 10+, 9+ and 8+ of the puffed Ne impurity. Beam 3 is most perpendicular to the LOS, all other beams from box 1 are turned off. NBI dips and radial plasma sweeps are applied to improve the data quality.

$n = 8 \rightarrow 7$  at 529.0 nm), which are not used, are also visible in the spectra. The steady-state approach with constant impurity densities supports a high data quality as it allows us to average data in time, to do NBI dips for subtraction of passive contributions to the spectra and to do radial plasma sweeps for measurements at more radial positions.

The evaluation of the spectral lines is illustrated in figure 3. It shows that even in the case where there are many passive lines around the active lines, cleaned spectra containing only the CX-lines can be retrieved. Fitting these with a Levenberg-Marquart minimization, the temperature, the toroidal velocity and the radiances can be obtained from the broadening, shift and intensities of the spectral lines. The fits are based on pre-calculated line shapes on a logarithmic temperature grid that can be interpolated. Doppler broadening, instrument function, Zeeman effect due to the B-field, and fine structure splitting are included in this computation. Since the signal-to-noise ratio is better for the  $\text{Ne}^{10+}$  data in the core and for the  $\text{Ne}^{8+}$  and  $\text{Ne}^{9+}$  data in the edge, the temperature fits of the other CX-lines are constrained to the fitted temperatures of these CX-lines  $\pm 100$  eV in the core and edge CXRS systems, respectively. This ensures that all spectral line fits have approximately the same temperatures at the same radial positions.

The  $\text{Ne}^{8+}$  CX-line can hardly be distinguished from the equivalent  $\text{O}^{8+}$  CX-line since the Doppler broadening differs only by 10% [16]. However, also the effective CX emission rates of these spectral lines are approximately the same as the atoms are Rydberg-like for the high principal quantum number (14) into which the CX takes place. Thus, the impurity density information retrieved according to equation (2.7) from the combined  $\text{Ne}^{8+} + \text{O}^{8+}$  spectral line when assuming  $\text{Ne}^{8+}$  rates can be attributed to the sum of the  $\text{Ne}^{8+}$  and  $\text{O}^{8+}$  densities. Therefore, the impurity transport solver in the forward model is additionally run for oxygen and the summed densities

are compared to the radiance data using the  $\text{Ne}^{8+}$  effective CX emission rates.

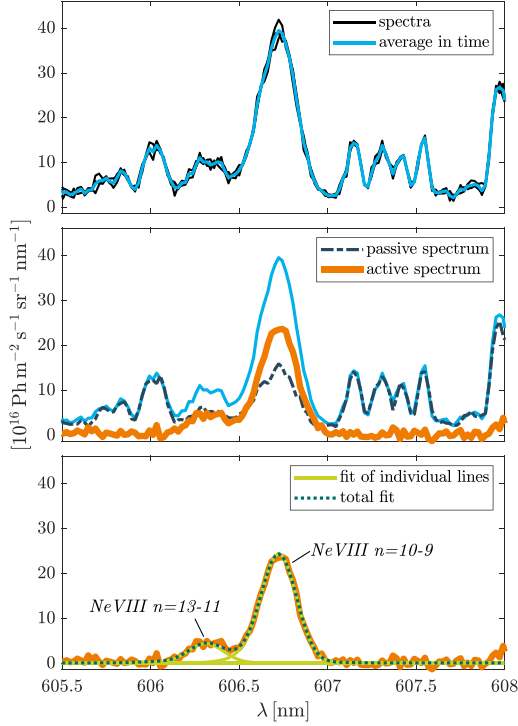
### 2.3. Forward model

In the following, the details of the forward model as sketched in figure 1 are presented.

**2.3.1. Plasma background.** Information on the background plasma profiles is important for the many atomic processes involved in the forward model and thus of particular relevance for the inference approach based on data from multiple charge states. Furthermore, comparative theoretical transport simulations, e.g. of neoclassical transport, also rely heavily on the kinetic profiles. However, accurately capturing the profiles in the steep gradient region of the pedestal is challenging.

**2.3.1.1. Main ion and electron background.** The electron density  $n_e$  and temperature  $T_e$  and the ion temperature  $T_i$  are fitted by an exponential cubic spline interpolation with manually selected spline knot positions. These fits are done with a simple  $\chi^2$  minimization. Their high accuracy could possibly be further improved using variable spline knot positions, as introduced for the analyses of the transport coefficient profiles in section 2.4. A similar Bayesian uncertainty quantification is however of limited use in this case, since including kinetic profile uncertainties in the transport coefficient inferences adds significant complexity.

The  $T_i$  fits are based on the temperatures obtained from the Ne CXRS measurements, which ensures good alignment with the impurity radiance data. The assumption of equal main ion and impurity temperatures is justified by the fact that the thermal equilibration is fast compared to transport time scales



**Figure 3.** Example of the evaluation of the observed spectra. The steady-state condition allows us to average spectra in time (top), subsequently, the passive spectra measured during the phases without NBI are subtracted (middle), and finally, the spectral lines are fitted taking the fine structure and Zeeman splitting into account (bottom).

[39]. We use the fits of the CX-lines with better signal-to-noise ratio in the core and edge respectively (cf section 2.2) and assign them to their emissivity-weighted mean radial position. Both the  $T_e$  and  $n_e$  fits use Thomson scattering data. For the  $T_e$  fit, the electron cyclotron emission (ECE) diagnostic can be used in addition, but the data are neglected outside an individually determined radial position, as they can suffer from ECE shine through in regions with small optical depth at the plasma edge. For the  $n_e$  fit, line-integrated density measurements from deuterium cyanide laser interferometry (DCN) are additionally used. Where good integrated data analysis (IDA) [40] profiles are available, they are used in the core, but the pedestal profiles are obtained directly from the diagnostic data. The edge diagnostics are shifted such that  $T_e$  is 100 eV at the separatrix, since it is known to be in the range 80–120 eV at AUG [4]. This shift is done equally in  $T_e$  and  $n_e$  to ensure good alignment.

**2.3.1.2. Thermal neutral deuterium.** It was first shown in [16] and confirmed in [22, 32] that recombination due to CX of impurity ions with recycling thermal neutral deuterium contributes significantly to the charge state balance at the plasma edge. It was also shown in [16] that although the CX processes may be local, this effect mostly acts globally on flux surfaces due to slow enough impurity reionization.

The flux surface averaged thermal neutral deuterium density  $n_{D^0}$  and temperature  $T_{D^0}$  are calculated with KN1D [41], a 1-D kinetic transport code for atomic and molecular hydrogen, in the KN1D OMFIT module. KN1D requires as inputs some simple SOL geometry specifications, similar to the Aurora SOL model (cf section 2.3.2), the electron and main ion background profiles as specified above, and the midplane molecular neutral pressure as is obtained from a pressure gauge.

However, merely the profile shape, but no absolute densities  $n_{D^0}$  can be obtained, since the recycling source at the edge is unknown. Therefore, an additional scalar parameter is introduced for the absolute density at the separatrix  $n_{D^0, \text{sep}}$ . Moreover, reflected particles can have other starting energies at the edge than the room temperature assumed in KN1D, which could impact the profile shape. However, the effect is estimated to be small based on the calculations presented in [16].

**2.3.1.3. Impurity content.** The beam attenuation calculation in the synthetic diagnostic includes collisions with impurities, which necessitates an estimate of the impurity content. Furthermore, the effective CX emission rate coefficients depend on the effective plasma charge  $Z_{\text{eff}}$ . At AUG,  $Z_{\text{eff}}$  is routinely determined via integrated data analysis [42] based on the bremsstrahlung background seen in the CXRS diagnostic. For the beam attenuation calculation, a fully stripped nitrogen density  $n_N$  is estimated as proxy for the impurity content such that  $Z_{\text{eff}}$  is matched together with the corresponding main ion density  $n_{D^+}$ .

**2.3.2. Impurity transport solver.** The forward model is based on the impurity transport solver Aurora [22, 23], which solves the system of transport equations, given in equation (2.4), for all charge states. It thus returns the charge state density profiles of the impurity when provided with diffusion and convection profiles. As additional inputs, it requires the magnetic equilibrium, the kinetic profiles  $T_i$ ,  $T_e$ ,  $n_e$ ,  $n_{D^0}$  and  $T_{D^0}$ , the rates for all relevant atomic processes affecting the charge state balance, and assumptions on the impurity sources and losses in the SOL.

**2.3.2.1. Ionization & recombination rates.** The source term in equation (2.4) is due to ionization and recombination processes from neighboring charge states, i.e.

$$Q_{I,Z} = - \left( n_e S_{I,Z} + n_e \alpha_{I,Z} + n_{D^0} \alpha_{I,Z}^{\text{CX}} \right) \cdot n_{I,Z} + n_e S_{I,Z-1} n_{I,Z-1} + \left( n_e \alpha_{I,Z+1} + n_{D^0} \alpha_{I,Z+1}^{\text{CX}} \right) \cdot n_{I,Z+1}, \quad (2.8)$$

where  $S$ ,  $\alpha$ , and  $\alpha^{\text{CX}}$  indicate the effective rate coefficients for ionization, radiative and di-electronic recombination, and recombination via CX with thermal neutral D (cf section 2.3.1). CX with NBI neutrals is not included, but plays a minor role in the pedestal due to small flux surface averaged beam densities [16].

For Ne,  $S$  is retrieved according to [43] and  $\alpha$  from the ADAS adf11 acd96\_ne file [44, 45]. The  $\alpha^{\text{CX}}$  data were calculated based on the CX cross sections for thermal deuterium with principal quantum numbers  $n = 1, 2, 3, 4$  [46, pp 172 and 174] together with the excited state populations due to electron impact excitation as provided by [47, appendix B]. To retrieve the CX rates with the recycling neutrals, the reduced temperature  $T_{\text{red}} = (T_i m_{D^0} + T_{D^0} m_i) / (m_{D^0} + m_i)$ , i.e. weighted by the neutral and impurity masses,  $m_{D^0}$  and  $m_i$ , is used.

**2.3.2.2. SOL model.** In the SOL, the radial coordinate cannot be calculated according to equation (2.2) since  $V$  is not defined. Therefore, the grid is extrapolated beyond the separatrix by approximating  $V$  based on the midplane flux surface width,  $\Delta R = R_{\text{LFS}} - R_{\text{HFS}}$ , i.e. the difference between the low and high field side midplane radii. To approximate  $V$  for a SOL flux surface, the separatrix shape is scaled up in the horizontal and vertical coordinates of the poloidal plane according to the ratio of  $\Delta R$  between the flux surface and the separatrix.

The neutral impurity distributions (of Ne and O) in the SOL, which are the sources of the ionized impurities, are calculated with Aurora's simple penetration model based on a specified neutral impurity source location and strength, particle starting energy and the neutral ionization rates. In addition to the radial transport, parallel transport in the SOL results in particle losses to the limiter and the divertor. These losses are calculated in Aurora from the plasma flow velocity specified by a Mach number together with geometry estimations on the radial extent of the SOL and limiters and the average connection lengths to the limiters and the divertor.

In this work, all options of Aurora's recycling model were disabled, instead the valve flux (of Ne) and the recycling fluxes (of Ne and O) are combined into the neutral impurity source strengths (of Ne and O). As these are unknown, two additional scalar parameters are added, i.e. a scaling factor of the Ne valve flux to account for the much higher recycling flux, and the neutral O particle source strength to model the oxygen content in the machine. All other quantities of the SOL model are fixed and their values used for all inferences presented in this paper are listed in table 3.

Because of these rather crude assumptions about SOL geometry, parallel transport and plasma-wall interaction, our framework is only able to infer reliable impurity transport coefficients within the confined plasma. We have ensured that the results do not depend crucially on the fixed SOL parameters (cf section 3.4).

**2.3.2.3. Algorithm.** Aurora is typically run with a numerical time evolution of the impurity charge state densities according to equation (2.4), using a finite-volume scheme [22]. However, specifically for inferences based on steady-state impurity densities, an analytic solution scheme was developed in [17], which is also implemented in Aurora. It includes the simple SOL model with impurity source and parallel loss terms as described above. Both options are available for use with this framework and were checked for consistency. Only if

Aurora's recycling model was used, small differences in absolute impurity densities could occur, as this is not included in the analytic solution scheme. The specific algorithmic choices used for all inferences presented in this paper are again listed in table 3.

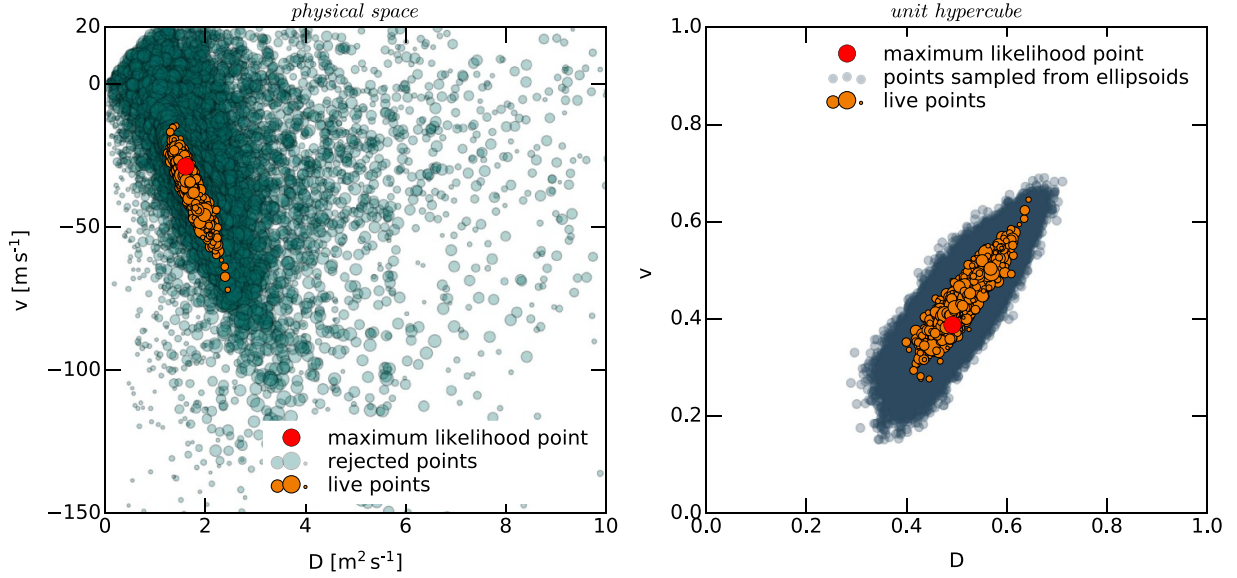
**2.3.3. Synthetic diagnostic.** The synthetic diagnostic maps the impurity charge state densities that are obtained with the impurity transport solver to the diagnostic data, i.e. the radiances of the CX-lines measured with CXRS, according to equation (2.7).

**2.3.3.1. NBI shape and attenuation.** The AUG beam shape, i.e. the beam density distribution without attenuation, is provided by an analytical beam model, whose parameters are determined to match spectroscopic beam emission measurements [48]. These densities are scaled according to the attenuation of the beam in the plasma, which is simulated with the collisional-radiative model COLRAD. This code was validated against experimental data in [49] and additionally provides the excitation state populations of the beam. With COLRAD, the beam attenuation can be calculated along several beamlets, but in this work only the attenuation along a single beamlet on the beam axis was used, as this was found to yield the same results as the multi-beamlet approach for our cases.

The collisional-radiative model includes mixing between excited states due to spontaneous decay according to Einstein rates and due to electron-, main ion- and impurity- impact excitation and de-excitation, as well as losses due to electron-, main ion- and impurity- impact ionization and due to main ion- and impurity- CX. Thus, the code is relying on  $n_e$ ,  $n_{D^+}$ ,  $T_e$ ,  $T_i$  and the impurity density, which is estimated as a fully stripped nitrogen density  $n_N$  from  $Z_{\text{eff}}$  (cf section 2.3.1). All rate coefficients are retrieved from [47, appendix B] and summarized in a matrix  $C$ , such that the time evolution of the beam excitation state populations  $\vec{f}$  is  $d\vec{f}/dt = C\vec{f}$  [47, appendix A]. In this work, 10 excited states are resolved and the truncation is compensated by increasing the losses from the highest resolved state by a factor of 8. All beam neutrals start in the ground state when arriving at the plasma and the equation is solved in discrete time steps, which are matched to positions along the beam according to the beam velocity determined from the beam energy. The numerical points along the beam are evenly spaced, and in this work 167 points are used.

The halo, i.e. the thermal neutral population that originates from the beam due to CX between beam neutrals and main ions, is also calculated at each discrete point along the beam. Its birth rate  $\vec{S}$  is obtained from excitation state resolved CX rates. The subsequent mixing of the excitation states due to spontaneous decay, due to electron-, main ion- and impurity- impact excitation and de-excitation, and due to CX with main ions (which produces new halo neutrals), and the losses due to electron-, main ion- and impurity- impact ionization and due to impurity- CX are again summarized in a matrix  $C_{\text{halo}}$ . Since the halo is assumed to be in equilibrium, the equation





**Figure 4.** Visualization of the sampling process (using case 8 in table 1 as example) with a 2-D cut through the parameter space, showing the transport coefficients at  $\rho_{\text{pol}} = 0.99$ . Left: Sampling history in physical space, i.e.  $v$  in  $\text{m s}^{-1}$ ,  $D$  in  $\text{m}^2 \text{s}^{-1}$ . Every third rejected point is shown, with the size of the dots increasing linearly with the iteration of their rejection, i.e. increasing with likelihood. The live points at sampling termination are plotted with the size of the dots now increasing linearly with logarithmic likelihood. Right: Sampling process in unit hypercube. Random samples from the current ellipsoids at sampling termination are plotted to indicate their combined shape. This inference was done without smoothness constraint in the prior, such that the mapping between unit hypercube and physical space is given by the univariate inverse prior CDFs (cf section 2.4.2).

$d\vec{f}/dt = C_{\text{halo}}\vec{f} + \vec{S}$  is solved as  $\vec{f} = -C_{\text{halo}}^{-1}\vec{S}$ . All atomic data are again retrieved from [47, appendix B]. The spatial distribution of the halo neutrals is obtained from interpolations of precalculated Monte Carlo simulations. This takes into account the approximate beam shape, the main ion CX and electron impact ionization rates of the halo, and the mean halo velocity according to  $T_i$  in each discrete point along the beam.

**2.3.3.2. Effective NBI CX emission rate coefficients.** As shown in equation (2.7), the CX reactions between the impurity ions and the NBI neutrals are summed over velocity components  $j$  and excitation states  $n$  of the neutrals. The sum over  $j$  includes the first 3 NBI energy components, i.e. with full,  $1/2$  and  $1/3$  beam energy, and the halo. The sum over  $n$  includes different principal quantum numbers of the NBI atoms. Given typical plasma parameters, most atoms are in the ground state and the fraction of atoms with  $n=2$  is only about 0.5% at its maximum along the NBI path, both for the beam and the halo. However, the effective CX emission rate coefficients are higher for the excited states. Therefore, only the  $n=1$  and  $n=2$  states of the beam neutrals and the  $n=2$  state of the halo neutrals contribute significantly, thus only these are included in the calculations.

The effective beam and halo CX emission rate coefficients  $\langle\sigma_{\text{CXline},n,j}v_j\rangle_{\text{eff}}$  for  $\text{Ne}^{8+}$ ,  $\text{Ne}^{9+}$  and  $\text{Ne}^{10+}$  are obtained as in [49] from interpolations of data calculated with the ADAS 309 code [44] for different  $n_e$ ,  $T_i$ ,  $Z_{\text{eff}}$  and NBI energies, assuming  $T_e = T_i$  and  $n_{D+}$  consistent with  $n_e$  and  $Z_{\text{eff}}$ . This code runs a collisional-radiative model to determine the principal quantum number populations and transitions based on adf01

data [45], which provides CX cross sections into different  $n$  and  $l$  quantum states.

**2.3.3.3. LOS integration.** As shown in equation (2.7), the product of the impurity and NBI beam densities with the effective CX emission rate coefficients is integrated along each LOS to forward model the line radiance. This means that the CXRS measurement is semi-local, in the sense that each LOS observes light emission from the small intersection region of the LOS and the beam. The more tangential the LOS is to the flux surfaces in this region, the narrower is the flux surface range contributing to the signal. In the inverse inference, this is equivalent to a small tomographic inversion, which becomes particularly relevant for less tangential LOS.

## 2.4. Inverse inference

In the following, the details of the Bayesian inverse inference, i.e. the sampling algorithm, and the prior and likelihood definitions, are presented. The inference is based on the CXRS data and the forward model, which are explained in sections 2.2 and 2.3, respectively. A visualization of the sampling process is shown in figure 4.

**2.4.1. Nested sampling.** According to Bayesian statistics, the probability of the parameters is defined by the normalized product of the prior probability and the data likelihood, as stated in equation (2.5). Due to the high dimensionality and complexity of the problem, an analytical calculation of the posterior probability distribution is not possible, rather

it needs to be sampled. Specifically for impurity transport inference, the nested sampling algorithm MultiNest [28, 29, 50] is suggested in [21]. In our framework, we use its version v3.10, wrapped with the python code PyMultiNest [51]. MultiNest is capable of handling complex, even multimodal, posterior shapes, which may arise due to the non-linearity of the model. Moreover, the algorithm does not rely on any gradient information, which would be prone to the round-off error of finite differences as long as the time-dependent numerical Aurora model is used [21]. In contrast to Markov Chain Monte Carlo (MCMC) methods, nested sampling also estimates the Bayesian evidence  $p(\mathcal{D}|\mathcal{M})$ , the normalization denominator in equation (2.5). As it represents the probability of the data integrated over the prior for a given model, i.e. the marginal likelihood, the applicability of different models can be compared by their evidence ratio, known as Bayes factor. This is a relative measure typically used in Bayesian model selection studies.

The key idea of nested sampling, first introduced by [26] and reviewed in [27, 52], is to draw uniform samples from the prior in regions with increasing lower boundary on the likelihood, i.e. nested shells in the simple case of increasing likelihood towards a central point. This is done with a live point set of size  $n_{\text{live}}$ , which is updated in each iteration by rejecting the sample with the lowest likelihood and replacing it by a sample with higher likelihood. Each sample (indexed by its rejection iteration  $i$ ) defines a region bounded below by its likelihood  $L_i$ , which contains the prior probability mass, called prior volume,  $x_i$ . Statistically, the prior volume shrinking factor  $x_i/x_{i-1}$  has the expectation value  $\exp(-1/n_{\text{live}})$ , thus,  $x_i = \exp(-i/n_{\text{live}})$  since  $x_0 = 1$ . This allows each sample to be assigned an average prior volume that it represents, called prior weight,  $w_i = (x_{i-1} - x_{i+1})/2$  [28], and a posterior weight  $p_i = (L_i w_i) / \sum_i (L_i w_i)$ . The samples together with their posterior weights approximate the posterior and can be used for visualization and calculation of different quantities, such as the mode of the distribution, i.e. the ‘maximum a posteriori’ (MAP) given by the sample with highest  $p_i$ , or univariate parameter distributions and their means.  $\sum_i (L_i w_i)$  is the Bayesian evidence.

In MultiNest, the samples are drawn uniformly in a unit hypercube space with each parameter ranging between 0 and 1. Subsequently, the hypercube sample  $\vec{s}_{\text{unit}}$  is transformed into the physical space sample  $\vec{s}_{\text{phys}}$ , respecting the prior mass conservation

$$\int p(\vec{s}_{\text{phys}}) d\vec{s}_{\text{phys}} = \int d\vec{s}_{\text{unit}}, \quad (2.9)$$

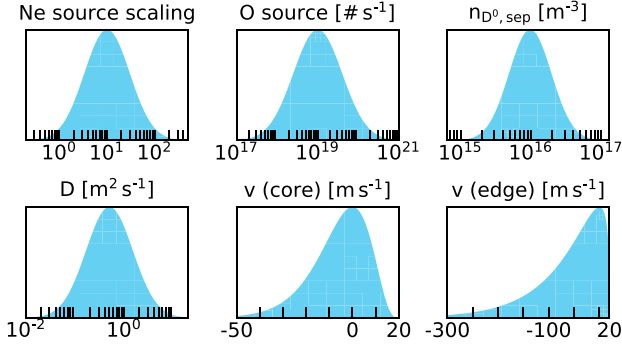
with the prior probability  $p$ , such that uniform samples from the prior are obtained. In case of univariate parameter priors, this is straightforward by applying their inverse cumulative distribution functions (CDFs). The task of sampling within likelihood-bounded regions is addressed via ellipsoidal rejection sampling, i.e. by drawing multiple ellipsoids around the current live point set, sampling within their boundaries, and rejecting any samples with too small likelihood.

However, such a region-based approach loses efficiency with increasing dimensionality [52], such that MultiNest can only easily handle up to  $\sim 30$  parameters [53]. As the inferences done with our framework are at the edge of this capability, we typically use MultiNest’s constant efficiency mode to ensure convenient inference times. This limits the size of the ellipsoids to meet a specified target sampling efficiency. It was found to yield reliable posterior distributions when applied in our framework (cf section 3), but can compromise the estimation of the Bayesian evidence. The tolerance factor for the logarithmic Bayesian evidence (stopping criterion) was set to 0.5, as recommended in [53]. Run with a target sampling efficiency of 0.05 as suggested in [53] and 1000 live points, a typical inference, like the one presented in section 4, requires  $\sim 500$  core hours on IPP’s TOK batch cluster, which provides nodes with 2 Intel Xeon Gold 6130 (Skylake) CPUs each. As the inferences can be run using MPI parallelization, the amount of time needed on such an HPC cluster is manageable. However, for good performance, the specifications of prior and likelihood presented below are of crucial importance.

**2.4.2. Prior.** The prior probability  $p(\mathcal{P}|\mathcal{M})$  should represent the prior knowledge on the parameters that are inputs of the forward model. These are in particular the transport coefficient profiles, the neutral impurity sources and the thermal neutral deuterium density at the separatrix  $n_{D^0, \text{sep}}$  (cf figure 1).

In general, the framework provides the choice of a univariate normal, a log-normal, a uniform or a log-uniform prior distribution for each parameter, with mandatory and optional parameter boundaries for the uniform and normal distributions, respectively. In this work, the priors for the neutral impurity sources (of Ne and O) and  $n_{D^0, \text{sep}}$  are chosen as log-normal distributions to cover multiple orders of magnitude. The Ne source rate prior is based on the rate read from the gas valve shotfile. This rate is scaled with a scalar factor, whose prior maximum is chosen to be 10 to account for the high wall recycling of Ne. The  $n_{D^0}$  profile is calculated with KN1D and also scaled with a scalar factor, whose prior is specified such that  $n_{D^0, \text{sep}}$  is most likely around  $10^{16} \text{ m}^{-3}$ , which is a typical value. All priors are shown in figure 5.

The impurity transport coefficient profiles are parameterized by a piecewise monotonic cubic spline interpolation. This allows us to keep the number of free parameters small by using only a few spline knots in the core, but placing more spline knots specifically in the steep gradient edge region. As it restricts the possible profile shapes, this parameterization is part of the prior. Optional free parameters are the spline knot values and positions (implemented as in [54, pp 113–5]), but not their number. Since  $\frac{v}{D}$  is better constrained by the experimental data than  $v$  and  $D$  individually, the latter are spline parameterized to ensure reasonable, in particular smooth, profiles for all quantities  $v$ ,  $D$  and  $\frac{v}{D}$ . The strong constraint of  $\frac{v}{D}$  can be seen in the correlation of the physical live points in figure 4. In line with [21], the boundary conditions for the splines are chosen to be  $v(0) = 0$  and  $(\partial D / \partial r)|_{r=0} = 0$ . The former ensures that  $\frac{v}{D}|_{r=0} = 0$ , since this ratio determines the



**Figure 5.** Univariate prior probability distributions for the model parameters. Log-normal distributions are chosen for the scalar parameters and  $D$ , whereas a customized distribution is used for  $v$ , with stronger skewness in the edge ( $\rho_{\text{pol}} \geq 0.95$ ) than in the core ( $\rho_{\text{pol}} < 0.95$ ), reflecting the typical impurity density peaking.

total impurity density gradient (cf equation (4.2)), which vanishes on axis, and the latter prevents large scatter of the under-determined  $D$  on axis. Since  $D$  is a purely positive quantity, the spline interpolation is done on  $\ln D$ .

In case of poor data quality, in particular sparse data and systematic errors, profiles with unphysical undulations, which are caused by spline overshoots in areas with dense spline knots, can have high likelihoods. To mitigate this, an additional optional smoothness constraint can be applied by introducing radial distance dependent correlations in the prior of the spline knot values. These correlations are introduced using a Gaussian copula, so for the spline knot values of each profile, the unit hypercube sample  $\vec{s}_{\text{unit}}$  is transformed as

$$\vec{s}_{\text{unit}} = \text{CDF}_{\mathcal{N}(0,1)} \left( \sqrt{M_{\text{cov}}} \cdot \text{CDF}_{\mathcal{N}(0,1)}^{-1}(\vec{s}_{\text{unit}}) \right), \quad (2.10)$$

with

$$M_{\text{cov}}^{i,j} = e^{-\frac{1}{2} \left( \frac{|\rho_{\text{pol},i} - \rho_{\text{pol},j}|}{\lambda_{\rho_{\text{pol}}}} \right)^2}. \quad (2.11)$$

The CDF of the normal distribution with mean 0 and standard deviation 1 ( $\mathcal{N}(0,1)$ ) is applied element-wise to  $\vec{s}_{\text{unit}}$ . However, the product with the square root of a covariance matrix  $M_{\text{cov}}$  with radial correlation length  $\lambda_{\rho_{\text{pol}}}$ , which introduces the correlations, is a multidimensional transformation. This breaks the direct traceability of the mapping between the original unit hypercube and the physical parameter space. In the sampling process shown in figure 4, which was done without smoothness constraint, this immediate mapping is retained.  $\lambda_{\rho_{\text{pol}}}$  can be adjusted individually for each inference, depending on the data quality.  $\sqrt{M_{\text{cov}}}$  is a matrix  $A$  such that  $M_{\text{cov}} = AA^T$ . It is computed via Cholesky decomposition, or alternatively, via eigendecomposition.

After performing the Gaussian copula correlation in unit hypercube space, each spline knot value is transformed into a physical parameter by applying the inverse CDF of its univariate prior distribution. In this work, a log-normal distribution is

used for  $D$ , as shown in figure 5. For  $v$ , especially in the pedestal, negative values are much more likely than positive values due to the typically observed peaked impurity density profiles, which are due to inward convection. Therefore, a special skewed prior distribution is used, which, however, still covers flat or even hollow impurity density profiles:

$$p(v, \alpha, \beta) = \frac{\beta^\alpha (-v + v_{\text{max}})^{\alpha-1} e^{\beta(v+v_{\text{max}})}}{\Gamma(\alpha)}, \quad (2.12)$$

with

$$\alpha = \frac{\left( 2 \frac{\sigma_v^2}{v_{\text{max}}^2} + 1 + \sqrt{4 \frac{\sigma_v^2}{v_{\text{max}}^2} + 1} \right)}{2 \frac{\sigma_v^2}{v_{\text{max}}^2}}, \quad (2.13)$$

$$\beta = \frac{\alpha - 1}{v_{\text{max}}}.$$

This is a gamma distribution, mirrored around 0, and shifted such that the maximum possible value is  $v_{\text{max}}$ , the standard deviation is  $\sigma_v$ , and the maximum probability is at  $v=0$ . In this work,  $v_{\text{max}}$  is chosen as  $20 \text{ m s}^{-1}$ , and  $\sigma_v$  as  $12.5 \text{ m s}^{-1}$  in the core and  $75 \text{ m s}^{-1}$  in the edge.

If  $v$  and  $D$  are sampled independently, physically reasonable values of  $\frac{v}{D}$  cannot be ensured. To achieve this,  $v$  can be sampled not directly from the above presented univariate prior distribution, but conditionally on the value of  $D$  if the spline knot positions of the profiles are set to be equal. A maximum and standard deviation are therefore also defined for  $\frac{v}{D}$ , in this work  $\frac{v}{D}_{\text{max}}$  is  $20 \text{ m}^{-1}$ , and  $\sigma_{\frac{v}{D}}$  is  $12.5 \text{ m}^{-1}$  in the core and  $75 \text{ m}^{-1}$  in the edge, as for  $v$ . Then, for each sample, the prior from which  $v$  is sampled is adapted based on the value of the sample for  $D$ , such that the constraints for  $v$  and  $\frac{v}{D}$  are respected, i.e.

$$v_{\text{max,samp}} = \min \left( v_{\text{max}}, \left( \frac{v}{D} \right)_{\text{max}} \cdot D_{\text{samp}} \right), \quad (2.14)$$

$$\sigma_{v,\text{samp}} = \min \left( \sigma_v, \sigma_{\frac{v}{D}} \cdot D_{\text{samp}} \right).$$

Thus, the total univariate prior distribution for  $v$ , which is shown in figure 5, is the integral of the conditional prior for  $v$  over the prior for  $D$ :

$$p(v|\mathcal{M}) = \int p(v|D, \mathcal{M}) p(D|\mathcal{M}) dD. \quad (2.15)$$

The conditional prior is evident in the rejected samples in physical space in figure 4, e.g. the top left region does not contain any samples as they are excluded by the constraint on the maximum of  $\frac{v}{D}$ .

The univariate priors for all parameters, as well as the Gaussian copula transformation and the conditional prior for  $v$ , all ensure the prior mass conservation stated in equation (2.9). Moreover, prior predictive checks confirmed that the prior covers the range of physically reasonable solutions.

**2.4.3. Likelihood.** The data likelihood  $p(\mathcal{D}|\mathcal{P}, \mathcal{M})$  defines the probability of observing the actual CXRS data based on the synthetic data that is calculated with the forward model from the parameters as ground truth (cf figure 1). Thus, it should represent the spectroscopic measurement error.

In this work, uncorrelated Gaussian measurement errors are used, which are estimated for each spectrometer channel individually via bootstrapping, i.e. from the standard deviation between the data and interpolations made from a subset of the data. In reality, systematic measurement errors can be present in addition to this random scatter, e.g. due to calibration issues of individual channels or spectrometers. These can be included either as additional inferred scaling parameters or by using a profile likelihood, i.e. automatically estimating and applying the best scaling parameters in each likelihood evaluation. However, the inclusion of systematic errors is not routinely done, rather only in the case of apparent data offsets, since it significantly complicates the sampling. Moreover, if the data quality of individual channels is obviously poor, their weight in the likelihood may also be reduced manually.

In principle, the likelihood can also be used to account for model errors, in particular in the background plasma profiles, the atomic data, and the NBI shape and attenuation. Since these induce radially correlated deviations of the synthetic data, they suggest a multivariate Gaussian with a radial correlation length as likelihood. However, such a likelihood significantly complicates the posterior space and consequently convergence of the MultiNest sampling to the maximum likelihood point could no longer be achieved in our tests. Yet, a simpler approach is used to avoid unreasonably small posterior distributions that arise if no correlations are assumed in the large data sets. Namely, the variance of all data acquired by one spectrometer channel is scaled by the total number of data points acquired by that channel. The weight of the total data of each channel in the posterior is then equal to the weight of a single data point with the original variance. This approximation broadens the posterior distribution and, due to the general smoothness constraints in the prior (cf section 2.4.2), in particular increases the probability of radially correlated offsets.

## 2.5. OMFIT ImpRad module

The presented framework is embedded in the OMFIT [25] module ‘ImpRad’, which is designed for modeling of impurity radiation and inferences of impurity transport based on Aurora. Its graphical user interface facilitates the setting of the required Aurora parameters, sampler configuration, and prior and likelihood specifications, as well as the visualization of settings, diagnostic data, sampling, and results.

## 3. Methodology tests

### 3.1. Setup and general validation

In order to assess the capabilities of the framework, we conducted tests with the method of manufactured solutions, based on the QCE discharge presented in section 4, AUG #39461. Aurora was run with the plasma equilibrium and background

of this discharge and reasonable choices for the fixed parameters, which are listed in table 3. Realistic, i.e. not just spline-interpolated, transport coefficient profiles were used as ground truth.  $v$  was chosen close to the neoclassical profile, and  $D$  such that there is a transport barrier in the pedestal, but the diffusion remains above the neoclassical value, as could be expected for the QCE regime based on our results in section 4. For the other free parameters, the ground truth values were chosen close to the inference result in section 4.2. A synthetic data set was generated according to the pattern of the original data, i.e. with the same amount of data at the same LOS positions, as shown in figure 12. The percentage errors of the original data were determined via bootstrapping (cf section 2.4.3) and applied to the synthetic data as univariate Gaussian perturbations. In addition, realistic calibration offsets similar to those inferred in section 4.2 were introduced for both edge spectrometers and added as free parameters, with Gaussian priors around the values that can be estimated by eye from the blank data set. All other priors and the likelihood were chosen as stated in section 4.2. Figure 6 also shows the ground truth and the priors.

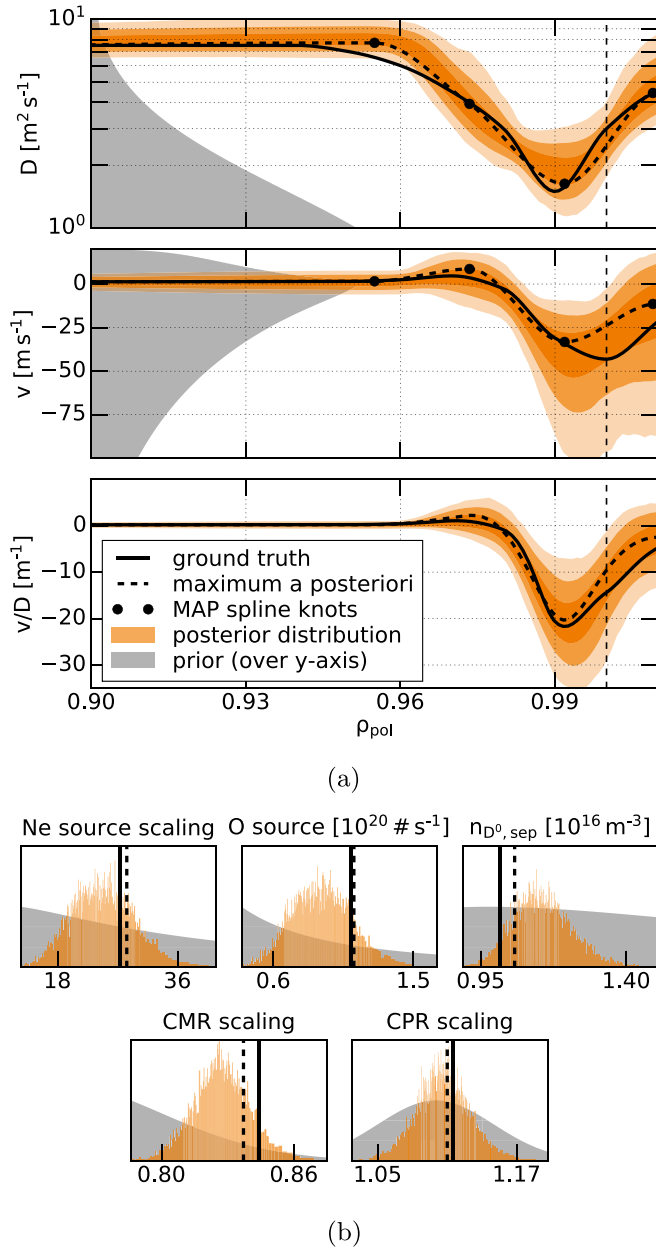
All tests are summarized in table 1 for comparison with their Bayes factors and quantities to measure the data match and accuracy of the MAP (‘maximum *a posteriori*’, cf section 2.4.1). The inferences were performed in MultiNest’s constant efficiency mode with a target sampling efficiency of 0.05 and 1000 live points. The stability of the posterior against these sampler settings was tested for the reference inference (case 1), which was repeated with a sampling efficiency of 0.01 and with 1500 live points, both of which yielded consistent results. This reference inference, which has the best MAP data match and accuracy, is shown in figure 6 and demonstrates that our framework is able to reconstruct the correct  $D$  and  $v$  profiles and additional free parameters from a typical data set. It was also repeated without Ne<sup>9+</sup> data (case 2), providing a similar posterior and proving that data from 2 charge states is in principle sufficient for an inference.

The following tests are aimed at assessing the spline parameterization of the transport coefficient profiles and the influence of data perturbations and model errors on the inference. However, it should be noted that this study remains selective as not all possible settings and influences can be tested. Moreover, the Bayes factors (cf section 2.4.1) are used for comparison, employing the Jeffreys’ scale [55, appendix B], according to which a Bayes factor of  $\gtrsim 3$  indicates substantial evidence for the model with higher Bayesian evidence. In doing so, we must bear in mind that the accuracy of the Bayesian evidence estimates is compromised by the use of MultiNest’s constant efficiency mode (cf section 2.4.1). Thus, the values shown in table 1 should be taken as indicative rather than relying on their absolute values.

### 3.2. Assessment of the spline parameterization

The inference from the synthetic data was repeated with different settings for the spline knot locations and the smoothness prior of the  $D$  and  $v$  profiles, listed in table 1. This model selection test in particular suggests not to use too few





**Figure 6.** Inference from synthetic data with the setup of the reference case, specified in table 1. (a) Transport coefficient profiles at the plasma edge. The orange shadows indicate the 1, 2 and 3  $\sigma$ -quantiles of the posterior probability distribution, i.e., in the non-Gaussian case the ranges covering 68.3 %, 99.4% and 99.7% of the probability, likewise to both sides of the probability mean. The normalized prior distributions are plotted over the y-axis. The vertical dashed line indicates the separatrix. (b) Additional scalar parameters. The posterior probability distributions (orange) and the normalized prior distributions (grey) are shown. The ground truth (solid) and the MAP (dashed) are indicated by vertical lines (black).

spline knots (case 4), and not to apply a too strong smoothness prior (case 7). The use of free knots is slightly more favorable than fixed knots (case 8 vs. case 1) and the positions of the fixed knots are also slightly relevant (good positions, i.e. close to the MAP from case 1, in case 8 and worse positions in case 9). That none of this is strongly indicated, can be understood by the high number of knots, which are densely packed

in the pedestal in all three cases. Furthermore, the test indicates that the reference case 1 is using the optimum number of spline knots, as both the removal (case 3) and the addition (case 5) of knots reduces the evidence, the latter probably due to an unnecessary increase of the parameter space dimensionality. Finally, the use of a weak radial correlation length for the smoothness prior (case 6) seems to be slightly suggested by the Bayes factor, but its application results in a worse MAP data match and accuracy. This can be understood as the good data quality, i.e. dense data without systematic errors, does not pose any risk of spline overshoots. Additional imposed smoothness is therefore not necessary, but rather hinders the capture of the actual profiles. In summary, the presented inferences show that the framework is able to handle a sufficient number of spline knots in the pedestal to capture profile shapes of realistic complexity. Moreover, the inference quality is not severely degraded when a small smoothness prior is imposed, which may be useful in the case of poorer data quality.

### 3.3. Influence of data perturbations

In the inferences presented above, the error pattern of the synthetic data matches the likelihood definition exactly. In reality, however, data perturbations that are not captured in the likelihood can occur. In the case of our CXRS data, such perturbations are most likely systematic errors in the form of calibration issues of individual channels, which are difficult to correct or infer as free parameters, as they are often not well constrained by the profile shape. Therefore, the reference inference, case 1 in table 1, shown in figure 6, was repeated with realistic additional channel offsets (case 10). The offsets were chosen as they were found in the original data, i.e. the inverse factors to those used for data correction in section 4.2 (CMR-1-2 $\times$ 0.90, CMR-1-10 $\times$ 1.30, CMR-1-11 $\times$ 0.85) were applied. The comparison of the transport solution with the reference case is presented in figure 7, column 1. It shows the sensitivity of the inferred diffusion profile and stresses the importance of accurate calibrations.

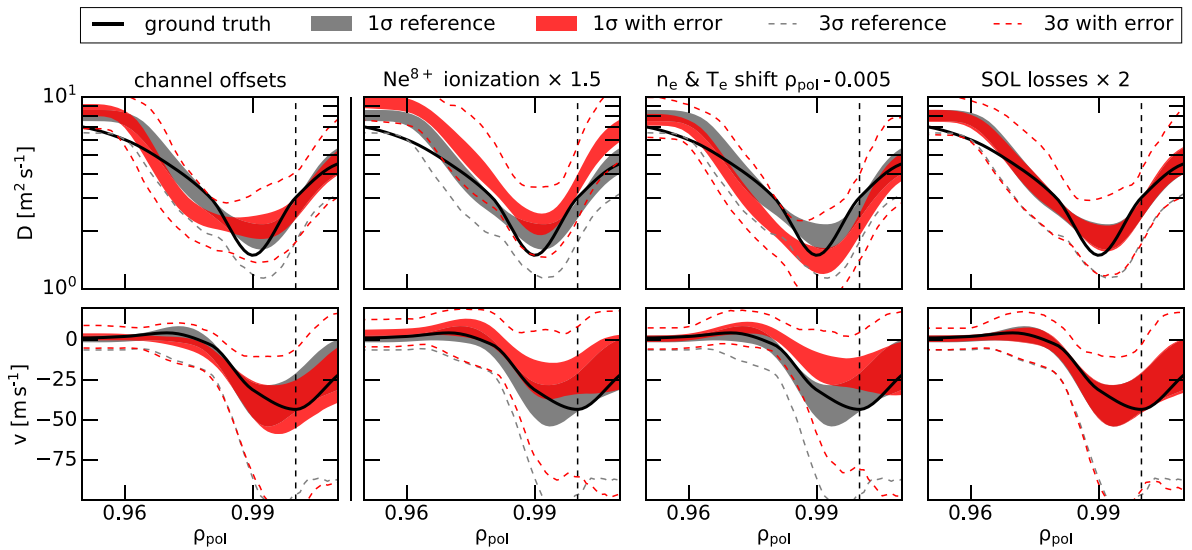
### 3.4. Influence of model errors

In the inferences presented above, no model error was assumed, although it could exist in the background plasma profiles, the atomic data, the SOL model, or the NBI shape and attenuation. For our inferences based on data from multiple charge states in the steep gradient region of the pedestal, particularly important error sources are the ionization and recombination rates used in Aurora since they affect the impurity charge state balance. These are retrieved from sophisticated atomic data (cf section 2.3.2) together with the kinetic plasma profiles (cf section 2.3.1), mainly  $T_e$ , which are difficult to determine with good alignment in the pedestal. Moreover, due to the proximity of the SOL, it is essential to ensure that the results do not depend crucially on the exact settings for the fixed parameters in the approximate SOL model (cf section 2.3.2). For these reasons, the reference inference, case 1 in table 1, shown in figure 6, was repeated with artificially introduced



**Table 1.** Comparison of inferences from synthetic data with different settings. In the reference case (1), 4 knots are placed in the core, which are free to move between minimum boundaries of  $\rho_{\text{pol}} = 0.05, 0.1, 0.35, 0.75$  and maximum boundaries of  $\rho_{\text{pol}} = 0.25, 0.65, 0.9, 0.95$ , and another 4 knots are placed in the edge, which are all free to move in the range  $0.95 < \rho_{\text{pol}} < 1.03$ , keeping a minimum distance of  $\rho_{\text{pol}} = 0.01$  and bounded from above by a fixed knot at  $\rho_{\text{pol}} = 1.03$ . Also, in the reference case, the smoothness prior with radial correlation length  $\lambda_{\rho_{\text{pol}}}$  (cf section 2.4.2) was disabled. The Bayes factors (cf section 2.4.1) can only be compared for inferences with the same likelihood, i.e. especially when using the same data set. The data match and the accuracy of the MAP in the pedestal ( $0.95 < \rho_{\text{pol}} < 1.0$ ) are measured by the reduced  $\chi^2$ , where  $n_{\text{DOF}} = n_{\text{data}} - n_{\text{parameters}}$ , and by the mean squared deviation of the  $v$  and  $D$  profiles from the ground truth, weighted by half the size of the posterior  $1\sigma$ -quantile (cf figure 6).

Settings	Bayes factor	ped. MAP $\frac{\chi^2}{n_{\text{DOF}}}$	ped. $\left( \frac{v_{\text{MAP}} - v_{\text{truth}}}{\sigma_{v,\text{post.}}} + \frac{D_{\text{MAP}} - D_{\text{truth}}}{\sigma_{D,\text{post.}}} \right)^2$
(1) reference case	1.00	1.05	0.05
(2) as (1), but without $\text{Ne}^{9+}$ data	not comparable	1.09	0.09
(3) $-1$ edge knot	0.56	1.15	0.18
(4) $-2$ edge knots	0.05	1.21	0.31
(5) $+1$ edge knot	0.36	1.11	0.15
(6) $+\lambda_{\rho_{\text{pol}}} = 0.01$	3.21	1.10	0.12
(7) $+\lambda_{\rho_{\text{pol}}} = 0.03$	0.09	1.25	0.26
(8) Fixed edge knots at $\rho_{\text{pol}} = 0.96, 0.975, 0.99, 1.01$	0.63	1.09	0.05
(9) Fixed edge knots at $\rho_{\text{pol}} = 0.965, 0.98, 0.995, 1.015$	0.43	1.13	0.21
(10) with channel offsets	not comparable	1.65	0.11
(11) $\text{Ne}^{8+}$ ionization $\times 1.5$	$5.11 \cdot 10^{-5}$	1.13	0.31
(12) $n_e$ & $T_e$ shift $\rho_{\text{pol}} - 0.005$	0.65	1.07	0.27
(13) SOL losses $\times 2$	0.95	1.11	0.07



**Figure 7.** Inferences from data with realistic channel offsets (column 1) or with different types of model errors (columns 2–4), compared to the reference inference (case 1 in table 1, shown in figure 6).

model error according to the following model modifications (cases 11, 12 and 13):

- $\text{Ne}^{8+}$  ionization rates  $S$  increased  $\times 1.5$
- $n_e$  and  $T_e$  shifted inward by  $\rho_{\text{pol}} = -0.005$
- SOL Mach number, i.e. parallel losses, increased  $\times 2$

The comparisons of the transport solutions with the reference case are presented in figure 7, columns 2–4. They show that

the profiles are indeed mostly independent of the SOL losses, but sensitive to inaccuracies in the atomic data and in the kinetic profiles. The increased SOL losses were found to be compensated by a reduction of the diffusion coefficient in the far SOL, where it is not constrained by CXRS data. This region is not shown in figure 7, and does not affect the pedestal. In another test, a change of the impurity source positions from 4.5 cm to 3 cm outside the separatrix also showed no influence on the pedestal result, but was counterbalanced by slightly

reduced inferred source strengths. Potential model errors in the synthetic diagnostic (cf section 2.3.3) were not tested. However, [16] showed that the error in the beam attenuation can be estimated to be, at most, 15% and the error in the relative effective CX emission rate coefficients when comparing two ionization states to be, at most, 20%.

## 4. Impurity transport in a QCE discharge

### 4.1. Discharge design

The framework was applied to infer the Ne transport coefficients in the QCE regime discharge AUG #39461. This discharge was in steady state in the time interval 3.95–6.81 s used for our analysis. Important plasma parameters in this time interval are summarized in table 2. A high density with a high gas puff rate, and a high shaping were used to access the QCE regime. The equilibrium was calculated at 5.38 s. AUG had been boronized two shot days previous to the discharge, yielding a rather low oxygen content in the plasma. The ELM time trace and relevant plasma profiles are shown in figures 8 and 9. It should be noted that  $T_e$  at the separatrix was fixed to 100 eV in the fit ( $n_{e,sep} = 4.4 \cdot 10^{19} \text{ m}^{-3}$ ), which is motivated by the QCE database presented in [34]. However,  $T_{e,sep}$  and  $n_{e,sep}$  vary within different QCE discharges, thus  $T_{e,sep}$  could be lower, as presented in [5] and [36]. Such different values could impact the analysis result, as demonstrated in section 3.4.

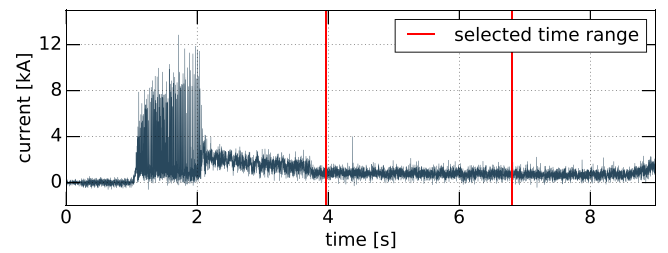
The CXRS LOS were arranged in the configuration for the 2021 experimental campaign, i.e. grouped into 45 core LOS from one optical head (CER) and 22 edge LOS from two optical heads (CMR-1, CMR-2) looking toroidally onto the NBI beam 3. The standard setup for the LOS connection to the spectrometer channels in the 2021 campaign was modified for our purpose prior to the experiment by distributing the LOS of the edge system alternately on two spectrometers (CMR and CPR). This involved a dis- and re-connection of the LOS imaged onto the CPR spectrometer, measuring the  $\text{Ne}^{10+}$  edge data. The core LOS were imaged on two spectrometers (CAR and CER) by default.

The spectrometer characteristics, the geometry of all LOS, and the LOS transmissivities plus the absolute intensity measurements of the spectrometer channels are routinely calibrated. The latter in particular is repeated before and after each campaign due to possible degradations of the optical system. In the 2021 campaign, no significant degradation was observed for the core CXRS system, whereas the edge system suffered some degradation, especially for those fibers that had been dis- and re-connected during the campaign. Therefore, the post-campaign intensity calibration was used, as #39461 was done towards the end of the campaign.

To improve the spectroscopic data quality, the NBI beam 3, which was operated at a beam voltage of 58.9 kV and an injection power of 2.4 MW, was switched on in phases of 230 ms, with dips of 70 ms without beam operation in between. This allows the subtraction of passive contributions to the spectra. Additional NBI power was provided on the other side of the torus (NBI box 2 with beam 8 in blips opposite to those of

**Table 2.** Plasma parameters in #39461 in the stationary phase 3.95–6.81 s.

Parameter	Value
$I_p$	0.8 MA
$B_T$	–2.5 T
D gas puff rate	$2.4 \cdot 10^{22} \text{ els}^{-1}$
Ne gas puff rate	$10^{21} \text{ els}^{-1}$
Ne gas valve	divertor valve Du01X
ICRF heating	—
ECRH power	1.6 MW, 3 gyrotrons
NBI power	4.9 MW
$W_{\text{MHD}}$	0.49 MJ
upper triangularity $\delta_{\text{up}}$	0.27
Greenwald fraction $n/n_{\text{GW}}$	0.89



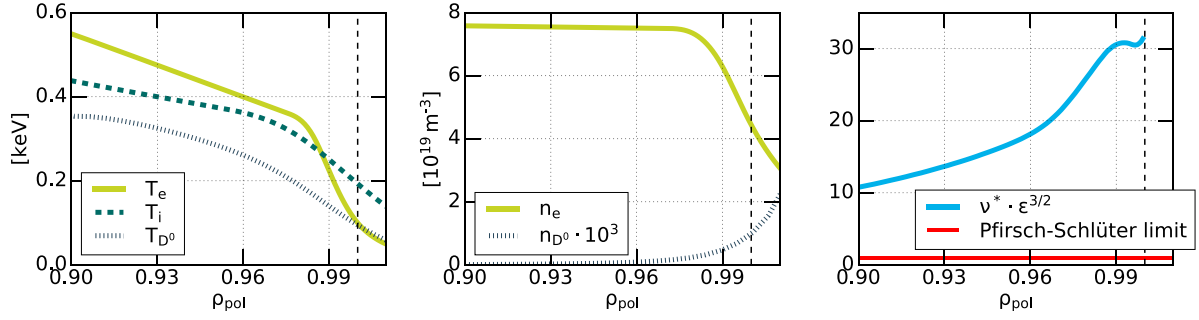
**Figure 8.** Outer divertor shunt current (ELM proxy) in #39461. The time range that is used for the data analysis is marked with vertical bars.

beam 3 to ensure approximately constant heating power, and beam 5 continuously, both with about 2.5 MW). Moreover, to increase the radial density of the measurements, a radial plasma sweep was done, shifting the separatrix from a radial position of 2.138 m–2.128 m and back in steps of 2 and 1 mm, respectively, where after each step data were taken for 300 ms.

All spectrometers were set to 5 ms integration time, and the spectra acquired on each channel, i.e. LOS, were averaged in groups of 3 after being sorted by their radial position according to the plasma sweep.

### 4.2. Data analysis

For the impurity transport analysis, the fixed Aurora parameters were chosen as specified in table 3, and the prior and likelihood as stated in sections 2.4.2 and 2.4.3, and detailed below. The spline parameterization settings were equal to those used in the reference case in table 1. Also here, this number of edge spline knots had the best Bayesian evidence and the posterior was stable with respect to an addition of knots, and due to the very good data quality, no smoothness constraint via radial spline knot correlations in the prior was needed. Only three channels showed small calibration offsets, which were manually corrected: CMR-1-2  $\times 0.90$  ( $\text{Ne}^{10+}$  at  $R = 2.104 \text{ m}$ ), CMR-1-10  $\times 1.30$  ( $\text{Ne}^{10+}$  at  $R = 2.120 \text{ m}$ ) and CMR-1-11  $\times 0.85$  ( $\text{Ne}^{8+}$  and  $\text{Ne}^{9+}$  at  $R = 2.123 \text{ m}$ ). This was possible due to the large radial plasma sweep, which resulted in good radial overlap of data points from adjacent channels. Moreover, scaling factors were inferred for both edge spectrometers (CMR and CPR) as calibration offsets were



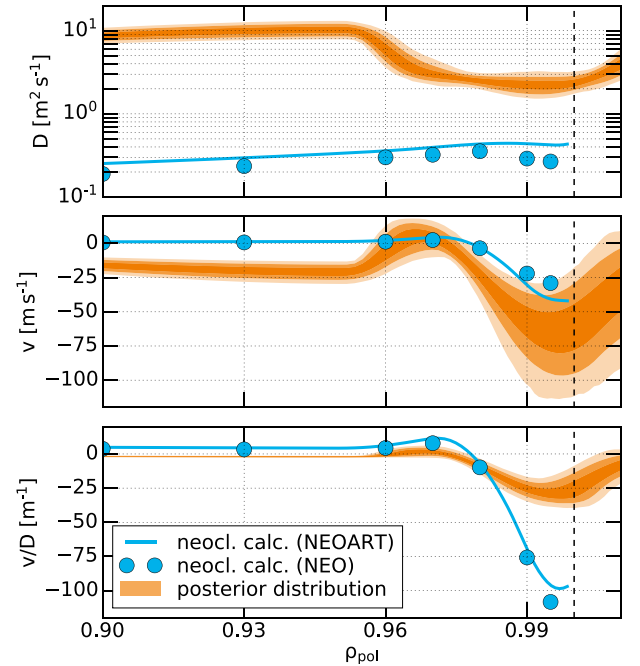
**Figure 9.** Relevant plasma profiles in #39461. Left: Electron, ion and thermal neutral deuterium temperatures.  $T_D$  is lower than  $T_i$  due to the main origin of thermal neutrals from further outward CX reactions. Middle: Electron and thermal neutral deuterium densities. Right: Collisionality  $\nu^*$  for Ne, compared to the Pfirsch-Schlüter limit at  $\nu^* \cdot \epsilon^{3/2} = 1$ , where  $\epsilon$  is the inverse aspect ratio.

**Table 3.** Aurora settings used in the methodology tests in section 3 and in the inference in section 4.2. For parameter definitions see [23] and [24]. All recycling options are turned off.

Parameter	Value
algorithm	steady-state analytical
radial grid: $k$ , $dr_0$ , $dr_l$	6.0, 1.0, 0.05
Ne & O neutral source energy	0.5 eV
distance of sources to separatrix	4.5 cm
decay length outside last grid point	1.0 cm
SOL Mach number	0.05
distance of last grid point to separatrix	9.0 cm
distance of limiters to separatrix	6.0 cm
connection length to limiters	0.5 m
connection length to divertor	29.4 m

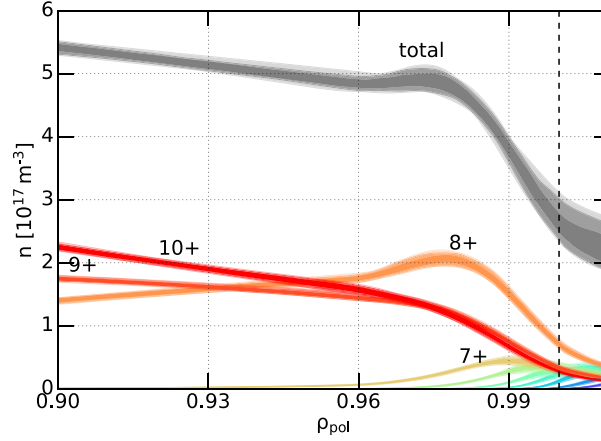
evident. Their priors were selected as Gaussians centered around values estimated by eye (0.75 and 1.1), both with a standard deviation of 0.05 and truncated at 0.5 and 1.5. The weight of the data in the univariate Gaussian likelihood was not only reduced according to the number of data points for a given channel, but the weight of all core LOS in the likelihood was additionally halved to give approximately equal weight to the data from the edge and the core CXRS systems.

Figures 10 and 11 show the posterior distribution of the Ne transport coefficient profiles and of the charge state distribution. The high inference quality is evident from the good data agreement of the MAP in figure 12. The MAP values of the scalar parameters are 28.04 for the Ne source scaling,  $1.10 \cdot 10^{20} \text{ s}^{-1}$  for the O particle source,  $0.94 \cdot 10^{16} \text{ m}^{-3}$  for  $n_{D^0, \text{sep}}$ , and 0.86 and 1.14 for the scaling of the CMR and CPR edge spectrometers, respectively. The  $Z_{\text{eff}}$  contribution of the inferred Ne concentration matches approximately the  $Z_{\text{eff}} \approx 1.6$  retrieved from integrated data analysis [42] (IDZ shotfile, cf section 2.3.1), which is used as an input to the framework (cf figure 1). Similar results were obtained when the inference was run based only on  $\text{Ne}^{8+}$  and  $\text{Ne}^{10+}$  data, indicating the consistency of the  $\text{Ne}^{9+}$  effective CX emission rate coefficients. Moreover, the inference outcome was well reproduced with increased sampling efficiency (0.01) and number of live points (1500), proving that the sampling is converged.

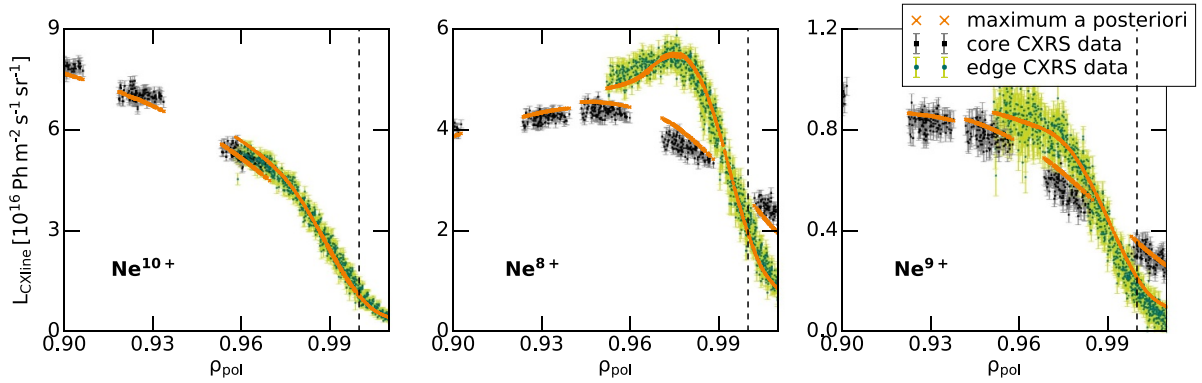


**Figure 10.** Inferred radial Ne transport coefficients at the plasma edge, showing the posterior distribution as in figure 6. The transport coefficient profiles are compared to neoclassical calculations, averaged over  $\text{Ne}^{8+}$ ,  $\text{Ne}^{9+}$  and  $\text{Ne}^{10+}$  according to their posterior mean densities. The pedestal reaches from  $\rho_{\text{pol}} \approx 0.97$  to the separatrix, indicated as vertical dashed line.

Figure 10 also compares the pedestal Ne transport results to neoclassical transport modeling with NEOART [56, 57] and NEO [58–60]. Both codes are capable of treating multi-species collisions, i.e. to include collisions between the different Ne charge states. This is particularly important given the high Ne concentration, which is above the trace limit. For the calculations, an additional small nitrogen concentration of 0.4% was assumed in order to match the  $Z_{\text{eff}}$  from IDZ exactly. Moreover, the low rotation limit was assumed, since Ne is light enough to be only marginally affected by poloidal asymmetries due to rotation. NEO was run on individual radial grid points, using the Miller extended harmonic equilibrium parameterization [61] including the first 6 Fourier harmonics. The resolution was increased beyond the default to 11 energy



**Figure 11.** Inferred Ne charge state densities at the plasma edge, showing the posterior quantiles as in figure 10. Decreasing charge states in rainbow colors, in grey the total Ne density summed over all charge states.



**Figure 12.** CXRS data with error bars overlaid with the MAP solution (pedestal  $\chi^2/n_{\text{DOF}} = 2.42$ ), for all 3 charge states. The  $\rho_{\text{pol}}$  positions shown are weighted by the emissivity  $\epsilon$ , i.e.  $\int_{\text{LOS}} \rho_{\text{pol}} \epsilon dl / \int_{\text{LOS}} \epsilon dl$ . Thus, the apparent ‘mismatch’ between core and edge LOS is a geometry effect, due to the more tangential view of the edge LOS, whereas the outermost core LOS are more influenced by the pedestal density decay. All inferred (MAP) or manually set data scaling parameters are applied.

polynomials, 30 polynomials in the cosine of the velocity pitch angle, and 25 points in the poloidal direction, to ensure convergence also close to the separatrix. The offset between the NEO and NEOART results at the very edge is mainly due to the classical transport contribution and due to collisions with Ne charge states  $\leq 7+$ , which are both not included in the NEO calculations. In addition, the applicability of the drift-ordering may be compromised at the edge. Due to the high ion density and low ion temperature, i.e. high collisionality, the neoclassical transport of Ne is in the Pfirsch-Schlüter regime throughout the whole pedestal (cf figure 9).

#### 4.3. Neon transport results

The analysis results presented in figure 10 show that the diffusion coefficient in the QCE pedestal is significantly larger than the neoclassical prediction. This additional transport flattens the total Ne density profile, shown in figure 11, resulting in a pedestal peaking factor

$$F_{\text{Ne}} = \frac{n_{\text{Ne}}(\rho_{\text{pol}} = 0.97)}{n_{\text{Ne}}(\rho_{\text{pol}} = 1.0)} \quad (4.1)$$

of only about 1.98, compared to a neoclassical peaking factor of about 3.95, calculated from the NEOART simulation. For the convection, it is not clear from the results, whether there is a significant anomalous contribution, due to the large error bars.

These results reflect the transport in the QCE regime averaged over its small type-II ELMs, which are too fast to be resolved by the CXRS diagnostic, as they occur with frequencies in the kHz range, while the minimal exposure time of the used cameras is around 2.5 ms. Recent investigations [35, 62] propose that the type-II ELMs are local high- $n$  ballooning modes located in a narrow region just inside the separatrix. Presumably, they cause filamentary transport across the separatrix which flattens the density and pressure gradient such that the type-I ELMs are suppressed as the peeling-ballooning boundary is not reached [63]. These findings are supported by the observation of the QCM in the same radial range [36], whose properties are consistent with ballooning modes [37]. Our results suggest that this additional transport in the QCE pedestal acts as enhanced diffusion on impurities. However, the exclusive localization at the pedestal foot is not clearly indicated in the inferred impurity transport. This is not due

to an inability of the data analysis to resolve sharp peaks in the transport coefficient profiles as it was shown in the methodology tests in figure 6 that such features can be captured. A direct comparison with impurity transport analyses in inter-ELM phases of type-I ELMs H-modes could help to further investigate the location of the additional impurity transport.

At AUG, the enhanced diffusion leads to a beneficial behavior, i.e. the absence of impurity accumulation, as the diffusion flushes impurities out. However, it depends on the impurity density profile whether diffusion leads to inward or outward transport. In the absence of impurity sources in the confined plasma, the inverse gradient scale length of the steady-state total impurity density is determined by the transport coefficients as

$$\frac{\partial \ln n_I}{\partial r} = \frac{1}{n_I} \frac{\partial n_I}{\partial r} = \frac{\nu}{D}. \quad (4.2)$$

Thus, the profile is hollow in the case of outward convection, or peaked in the case of inward convection. The diffusion always acts to flatten the profile, i.e. it transports impurities inwards in the former and outwards in the latter case. In future devices, in particular ITER and DEMO, the neoclassical convection in the pedestal is expected to be dominated by the temperature screening term causing outward transport, contrary to typical AUG conditions [7]. This is supported by recent observations in JET plasmas with high temperature pedestals [8, 64]. Therefore, hollow impurity profiles are expected if no additional dominant inward convective contribution is active, which is not evident from our results. The enhanced diffusive transport would then no longer be beneficial, but rather weaken the effect of the temperature screening. The relevance of this effect depends on the specific impurity since the neoclassical convection scales with the charge such that the outward screening will be stronger for high-Z elements, such as W. Moreover, it depends on the collisionality  $\nu^*$ , which determines the strength of the neoclassical transport. Compared to current devices,  $\nu^*$  will be lower at the pedestal top due to higher plasma core temperatures. The QCE regime at AUG has high  $\nu^*$  throughout, and cannot be tested with low pedestal top  $\nu^*$ . Thus, if the additional diffusion of impurities is significant not only at the pedestal foot, but also at the top, where collisional transport will be smaller in ITER and DEMO, its influence could be more dominant than in AUG. Such a conclusion cannot be proven experimentally based on our data, but it is compatible with the results presented above.

## 5. Discussion and conclusion

We introduced a novel framework for the quantification of pedestal impurity transport coefficients at AUG, with comprehensive uncertainty quantification via Bayesian inference. The analyses are based on radial profiles of CXRS radiance data. With a tailored diagnostic setup, multiple impurity charge states are observed in steady-state plasmas, which allows the separation of diffusion and convection contributions to the radial impurity transport.

Our framework meets all criteria that were suggested by [21] for the assessment of impurity transport coefficient inferences. It accounts for the possibility of non-Gaussian and multimodal posterior probabilities, we used model selection to determine an appropriate profile parameterization, and we tested it with realistic synthetic data generated from a realistic ground truth.

Yet, the spline parameterization constrains the *a priori* possible transport coefficient profiles, which can lead to systematic errors appearing as correlated residuals [21]. This problem can be overcome with non-parametric inference using Gaussian process regression, which infers the values at each grid point and imposes a smoothness prior via hyperparameters [17]. However, dealing with the consequently large parameter space dimensionality ( $\sim 200$  in [17]) is not possible with MultiNest, but favors the use of a gradient-based MCMC algorithm for posterior inference. This is possible with the analytical steady-state transport solver that was developed in [17], but becomes difficult with the time-dependent numerical algorithm due to the round-off error of finite differences. Yet, the time-dependent Aurora code has an implementation in JULIA that supports automatic differentiation, and future work could follow this idea. In our framework, instead, the possibility for time-dependent analyses is inherently retained, since the nested sampling is gradient-independent. Moreover, as shown in this paper, our framework, relying on MultiNest, is able to perform inferences with sufficiently dense spline knots in the pedestal to reconstruct complex transport coefficient profiles.

Nevertheless, with MultiNest being a region-based algorithm, typical inferences with many spline knots, i.e. a  $\sim 30$ -dimensional parameter space, are computationally expensive. Using the constant efficiency mode, robust posterior inference is still possible within reasonable time, but the Bayesian evidence estimates are compromised and the quality of model selection studies as those presented in section 3 is reduced. To facilitate the inference when using dense spline knots in the pedestal and to obtain more accurate evidence estimates, a potential option would be employing a nested sampling algorithm that uses a step-sampler [65] to sample within the likelihood-constrained contours. For example, UltraNest [66] could be a viable option. Using it in our framework is subject to ongoing research.

Future work could also include the implementation of further synthetic diagnostics to include more data in the inference, e.g. from SXR and vacuum ultraviolet spectroscopy. In particular, including data from lower charge states could help to reduce the uncertainty in the convection solution, if they are significantly present inside the separatrix as in figure 11. However, this might require a model for the Z-dependence of  $\nu$ , since the assumption of equal  $\nu$  for all observed charge states would be strongly violated when adding too small ionization states.

The presented analysis of radial Ne transport in a QCE discharge indicates enhanced diffusion above the neoclassical level in the pedestal and a consequently reduced Ne density peaking. Further experimental studies using our framework



are planned to validate these findings. Additionally, we intend to investigate other ELM-free confinement regimes and to compare to inter-ELM transport in type-I ELMy H-modes at AUG. A good extension would be experiments with Ar as impurity, which would allow us to scale the results to higher Z. However, this approach presents additional challenges, such as unknown effective CX emission rate coefficients and a helium line overlapping with the Ar<sup>16+</sup> CX-signal. Finally, ongoing improvements in gyrokinetic modeling for plasma edge turbulence, e.g. with GRILLIX [67], will help our understanding of the experimental results and pave the way towards pedestal impurity transport predictions for fusion reactors.



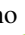





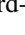
## Acknowledgments

This work has been carried out within the framework of the EUROfusion Consortium, funded by the European Union via the Euratom Research and Training Programme (Grant Agreement No 101052200 - EUROfusion). Views and opinions expressed are however those of the author(s) only and do not necessarily reflect those of the European Union or the European Commission. Neither the European Union nor the European Commission can be held responsible for them.

This material is based upon work supported by the U.S. Department of Energy, Office of Science, Office of Fusion Energy Sciences, under Award(s) DE-FC02-04ER54698. This report was prepared as an account of work sponsored by an agency of the United States Government. Neither the United States Government nor any agency thereof, nor any of their employees, makes any warranty, express or implied, or assumes any legal liability or responsibility for the accuracy, completeness, or usefulness of any information, apparatus, product, or process disclosed, or represents that its use would not infringe privately owned rights. Reference herein to any specific commercial product, process, or service by trade name, trademark, manufacturer, or otherwise does not necessarily constitute or imply its endorsement, recommendation, or favoring by the United States Government or any agency thereof. The views and opinions of authors expressed herein do not necessarily state or reflect those of the United States Government or any agency thereof.

Part of the data analysis was performed using the OMFIT integrated modeling framework [25].

## ORCID iDs

T. Gleiter  <https://orcid.org/0000-0001-7807-3048>  
 R. Dux  <https://orcid.org/0000-0002-3447-9553>  
 F. Sciortino  <https://orcid.org/0000-0002-5159-1889>  
 T. Odstrčil  <https://orcid.org/0000-0003-4173-4230>  
 D. Fajardo  <https://orcid.org/0000-0001-5802-4572>  
 C. Angioni  <https://orcid.org/0000-0003-0270-9630>  
 J. Buchner  <https://orcid.org/0000-0003-0426-6634>  
 R.M. McDermott  <https://orcid.org/0000-0002-8958-8714>  
 T. Hayward-Schneider  <https://orcid.org/0000-0003-0588-5090>

G.F. Harrer  <https://orcid.org/0000-0002-1150-3987>  
 M. Faitsch  <https://orcid.org/0000-0002-9809-7490>  
 M. Griener  <https://orcid.org/0000-0003-2953-536X>  
 R. Fischer  <https://orcid.org/0009-0000-6205-4731>  
 E. Wolfrum  <https://orcid.org/0000-0002-6645-6882>  
 U. Stroth  <https://orcid.org/0000-0003-1104-2233>

## References

- [1] Pütterich T., Fable E., Dux R., O'Mullane M., Neu R. and Siccino M. 2019 *Nucl. Fusion* **59** 056013
- [2] Kallenbach A. et al (the ASDEX Upgrade Team) 2013 *Plasma Phys. Control. Fusion* **55** 124041
- [3] Burrell K.H. 1997 *Phys. Plasmas* **4** 1499–518
- [4] Pütterich T., Dux R., Janzer M.A. and McDermott R.M. (the ASDEX Upgrade Team) 2011 *J. Nucl. Mater.* **415** S334–9
- [5] Faitsch M., Eich T., Harrer G.F., Wolfrum E., Brida D., David P., Griener M. and Stroth U. (the ASDEX Upgrade Team and the EUROfusion MST1 Team) 2021 *Nucl. Mater. Energy* **26** 100890
- [6] Viezzer E. et al (the EUROfusion WPTE Team and the ASDEX Upgrade Team) 2023 *Nucl. Mater. Energy* **34** 101308
- [7] Dux R., Loarte A., Fable E. and Kukushkin A. 2014 *Plasma Phys. Control. Fusion* **56** 124003
- [8] Field A.R. et al (JET Contributors) 2022 *Nucl. Fusion* **63** 016028
- [9] Hirshman S.P. and Sigmar D.J. 1981 *Nucl. Fusion* **21** 1079–201
- [10] Angioni C., Camenen Y., Casson F.J., Fable E., McDermott R.M., Peeters A.G. and Rice J.E. 2012 *Nucl. Fusion* **52** 114003
- [11] Bruhn C. et al (the ASDEX Upgrade Team) 2018 *Plasma Phys. Control. Fusion* **60** 085011
- [12] McDermott R.M., Angioni C., Cavedon M., Kappatou A., Dux R., Fischer R. and Manas P. (the ASDEX Upgrade Team) 2021 *Nucl. Fusion* **62** 026006
- [13] Sertoli M., Angioni C., Dux R., Neu R., Pütterich T. and Igochine V. (the ASDEX Upgrade Team) 2011 *Plasma Phys. Control. Fusion* **53** 035024
- [14] Pedersen T.S., Granetz R.S., Hubbard A.E., Hutchinson I.H., Marmar E.S., Rice J.E. and Terry J. 2000 *Nucl. Fusion* **40** 1795
- [15] Victor B.S. et al 2020 *Plasma Phys. Control. Fusion* **62** 095021
- [16] Dux R., Cavedon M., Kallenbach A., McDermott R.M. and Vogel G. (the ASDEX Upgrade Team) 2020 *Nucl. Fusion* **60** 126039
- [17] Nishizawa T. et al (the ASDEX Upgrade Team) 2022 *Nucl. Fusion* **62** 076021
- [18] Viezzer E., Pütterich T., Dux R. and McDermott R.M. (the ASDEX Upgrade Team) 2012 *Rev. Sci. Instrum.* **83** 103501
- [19] Howard N.T., Greenwald M., Mikkelsen D.R., Reinke M.L., White A.E., Ernst D., Podpaly Y. and Candy J. 2012 *Nucl. Fusion* **52** 063002
- [20] Griener B.A. et al (the DIII-D Team) 2015 *Phys. Plasmas* **22** 055901
- [21] Chilenski M.A., Greenwald M., Marzouk Y., Rice J.E. and White A.E. 2019 *Plasma Phys. Control. Fusion* **61** 125012
- [22] Sciortino F. et al 2021 *Plasma Phys. Control. Fusion* **63** 112001
- [23] Sciortino F. 2020 *Aurora documentation, release 1.0.0* (available at: <https://aurora-fusion.readthedocs.io>) (Accessed 19 August 2024)
- [24] Dux R. 2021 *STRAHL User Manual* Max-Planck-Institut für Plasmaphysik

- [25] Meneghini O. *et al* (the AToM Team) 2015 *Nucl. Fusion* **55** 083008
- [26] Skilling J. 2004 *AIP Conf. Proc.* **735** 395–405
- [27] Buchner J. 2023 *Stat. Surv.* **17** 169–215
- [28] Feroz F. and Hobson M.P. 2008 *Mon. Not. R. Astron. Soc.* **384** 449–63
- [29] Feroz F., Hobson M.P., Cameron E. and Pettitt A.N. 2019 *Open J. Astrophys.* **2**
- [30] Odstrčil T., Howard N.T., Sciortino F., Chrystal C., Holland C., Hollmann E., McKee G., Thome K.E. and Wilks T.M. 2020 *Phys. Plasmas* **27** 082503
- [31] Sciortino F. *et al* 2020 *Nucl. Fusion* **60** 126014
- [32] Sciortino F. *et al* 2021 *Nucl. Fusion* **61** 126060
- [33] Sciortino F. *et al* 2022 *Plasma Phys. Control. Fusion* **64** 124002
- [34] Faitsch M. *et al* (the ASDEX Upgrade Team and the EUROfusion MST1 Team) 2023 *Nucl. Fusion* **63** 076013
- [35] Harrer G.F. *et al* (the ASDEX Upgrade Team and the EUROfusion MST1 Team) 2022 *Phys. Rev. Lett.* **129** 165001
- [36] Griener M. *et al* (the ASDEX Upgrade Team and the EUROfusion MST1 Team) 2020 *Nucl. Mater. Energy* **25** 100854
- [37] Kalis J. *et al* (the ASDEX Upgrade Team and the EUROfusion MST1 Team) 2023 *Nucl. Fusion* **64** 016038
- [38] Viezzer E. *et al* (the ASDEX Upgrade Team) 2015 *Nucl. Fusion* **55** 123002
- [39] Viezzer E. *et al* (the ASDEX Upgrade Team) 2013 *Nucl. Fusion* **53** 053005
- [40] Fischer R., Fuchs C.J., Kurzan B., Suttrop W. and Wolfrum E. (the ASDEX Upgrade Team) 2010 *Fusion Sci. Technol.* **58** 675–84
- [41] LaBombard B. 2001 *KNID: A 1-D Space, 2-D velocity, kinetic transport algorithm for atomic and molecular hydrogen in an ionizing plasma* PSFC-RR-01-3 MIT Plasma Science & Fusion Center (available at: [https://library.psfc.mit.edu/catalog/reports/2000/01rr/01rr003/01rr003\\_abs.html](https://library.psfc.mit.edu/catalog/reports/2000/01rr/01rr003/01rr003_abs.html))
- [42] Rathgeber S.K., Fischer R., Fietz S., Hobirk J., Kallenbach A., Meister H., Pütterich T., Ryter F., Tardini G. and Wolfrum E. (the ASDEX Upgrade Team) 2010 *Plasma Phys. Control. Fusion* **52** 095008
- [43] Mattioli M., Mazzitelli G., Finkenthal M., Mazzotta P., Fournier K.B., Kaastra J. and Puiatti M.E. 2007 *J. Phys. B: At. Mol. Opt. Phys.* **40** 3569
- [44] Summers H.P. 2004 The ADAS user manual, version 2.6 (available at: [www.adas.ac.uk](http://www.adas.ac.uk))
- [45] OPEN ADAS 2024 (available at: <https://open.adas.ac.uk/>) (Accessed 19 August 2024)
- [46] Janev R.K. and Smith J.J. 1993 *Cross Sections for Collision Processes of Hydrogen Atoms With Electrons, Protons and Multiply Charged Ions (Atomic and Plasma-Material Interaction Data for Fusion vol 4)* (International Atomic Energy Agency (IAEA)) (available at: [www.iaea.org/publications/1839/atomic-and-plasma-material-interaction-data-for-fusion](http://www.iaea.org/publications/1839/atomic-and-plasma-material-interaction-data-for-fusion))
- [47] Geiger B. 2013 *Fast-ion Transport Studies Using Fida Spectroscopy at the ASDEX Upgrade Tokamak* (Dissertation Ludwig Maximilians Universität München)
- [48] Lebschy A. 2014 Electron density reconstruction using beam emission spectroscopy on a heating beam – a feasibility study *Master Thesis* Ludwig Maximilians Universität München
- [49] McDermott R.M. *et al* (the ASDEX Upgrade Team) 2018 *Plasma Phys. Control. Fusion* **60** 095007
- [50] Feroz F., Hobson M.P. and Bridges M. 2009 *Mon. Not. R. Astron. Soc.* **398** 1601–14
- [51] Buchner J. *et al* 2014 *Astron. Astrophys.* **564** A125
- [52] Ashton G. *et al* 2022 *Nat. Rev. Methods Primers* **2** 38
- [53] MultiNest Github Repository 2024 (available at: <https://github.com/farhanferoz/MultiNest>) (Accessed 17 November 2024)
- [54] Sciortino F. 2021 *Experimental Inference of Particle Transport in Tokamak Plasmas* (Dissertation Massachusetts Institute of Technology)
- [55] Jeffreys H. 1998 *The Theory of Probability* (Oxford Classic Texts in the Physical Sciences) (Oxford University Press)
- [56] Peeters A.G. 2000 *Phys. Plasmas* **7** 268–75
- [57] Dux R. and Peeters A.G. 2000 *Nucl. Fusion* **40** 1721
- [58] Belli E.A. and Candy J. 2008 *Plasma Phys. Control. Fusion* **50** 095010
- [59] Belli E.A. and Candy J. 2009 *Plasma Phys. Control. Fusion* **51** 075018
- [60] Belli E.A. and Candy J. 2011 *Plasma Phys. Control. Fusion* **54** 015015
- [61] Arbon R., Candy J. and Belli E.A. 2020 *Plasma Phys. Control. Fusion* **63** 012001
- [62] Radovanovic L., Dunne M.G., Wolfrum E., Harrer G.F., Faitsch M., Fischer R. and Aumayr F. (ASDEX Upgrade Team and the EUROfusion MST1 Team) 2022 *Nucl. Fusion* **62** 086004
- [63] Harrer G.F. *et al* (the EUROfusion MST1 Team and the ASDEX Upgrade Team) 2018 *Nucl. Fusion* **58** 112001
- [64] Garcia J. *et al* (JET Contributors) 2022 *Phys. Plasmas* **29** 032505
- [65] Buchner J. 2022 *Phys. Sci. Forum* **5** 46
- [66] Buchner J. 2021 *J. Open Source Softw.* **6** 3001
- [67] Zholobenko W., Zhang K., Stegmeir A., Pfennig J., Eder K., Pitzal C., Ulbl P., Griener M., Radovanovic L. and Plank U. (the ASDEX Upgrade Team) 2024 *Nucl. Fusion* **64** 106066